

# Search for cold gas in strong Mg II absorbers at $0.5 < z < 1.5$ : nature and evolution of 21-cm absorbers

N. Gupta<sup>1</sup>, R. Srianand<sup>2</sup>, P. Petitjean<sup>3</sup>, J. Bergeron<sup>3</sup>, P. Noterdaeme<sup>3</sup>, and S. Muzahid<sup>2</sup>

<sup>1</sup> ASTRON, the Netherlands Institute for Radio Astronomy, Postbus 2, 7990 AA, Dwingeloo, The Netherlands  
e-mail: gupta@astron.nl

<sup>2</sup> IUCAA, Post Bag 4, Ganeshkhind, Pune 411007, India

<sup>3</sup> UPMC-CNRS, UMR7095, Institut d'Astrophysique de Paris, F-75014 Paris, France

Received 2 March 2012; accepted 17 May 2012

## ABSTRACT

We report 4 new detections of 21-cm absorption from a systematic search of 21-cm absorption in a sample of 17 strong (rest equivalent width,  $W_r(\text{Mg II } \lambda 2796) \geq 1 \text{ \AA}$ ) intervening Mg II absorbers at  $0.5 < z_{\text{abs}} < 1.5$ . We also present 20-cm milliarcsecond scale maps of 40 quasars having 42 intervening strong Mg II absorbers for which we have searched for 21-cm absorption. These maps are used to understand the dependence of 21-cm detection rate on the radio morphology of the background quasar and address the issues related to the covering factor of absorbing gas. Combining 21-cm absorption measurements for 50 strong Mg II systems from our surveys with the measurements from literature, we obtain a sample of 85 strong Mg II absorbers at  $0.5 < z_{\text{abs}} < 1$  and  $1.1 < z_{\text{abs}} < 1.5$ . We present detailed analysis of this 21-cm absorption sample, taking into account the effect of the varying 21-cm optical depth sensitivity and covering factor associated with the different quasar sight lines. We find that the 21-cm detection rate is higher towards the quasars with flat or inverted spectral index at cm wavelengths. About 70% of 21-cm detections are towards the quasars with linear size,  $LS < 100 \text{ pc}$ . The 21-cm absorption lines having velocity widths,  $\Delta V > 100 \text{ km s}^{-1}$  are mainly seen towards the quasars with extended radio morphology at arcsecond scales. However, we do not find any correlation between the integrated 21-cm optical depth,  $\int \tau dv$ , or the width of 21-cm absorption line,  $\Delta V$ , with the LS measured from the milliarcsecond scale images. All this can be understood if the absorbing gas is patchy with a typical correlation length of  $\sim 30\text{-}100 \text{ pc}$ . We confirm our previous finding that the 21-cm detection rate for a given optical depth threshold can be increased by up to a factor 2 by imposing the following additional constraints: Mg II doublet ratio  $< 1.1$ ,  $W(\text{Mg II})/W(\text{Fe II}) < 1.47$  and  $W(\text{Mg I})/W(\text{Mg II}) > 0.27$ . This suggests that the probability of detecting 21-cm absorption is higher in the systems with high  $N(\text{H I})$ . We show that within the measurement uncertainty, the 21-cm detection rate in strong Mg II systems is constant over  $0.5 < z_{\text{abs}} < 1.5$ , i.e., over  $\sim 30\%$  of the total age of universe. We show that the detection rate can be underestimated by up to a factor 2 if 21-cm optical depths are not corrected for the partial coverage estimated using milliarcsecond scale maps. Since stellar feedback processes are expected to diminish the filling factor of cold neutral medium over  $0.5 < z < 1$ , this lack of evolution in the 21-cm detection rate in strong Mg II absorbers is intriguing. Large blind surveys of 21-cm absorption lines with the upcoming Square Kilometre Array pathfinders will provide a complete view of the evolution of cold gas in galaxies and shed light on the nature of Mg II systems and DLAs, and their relationship with stellar feedback processes.

**Key words.** quasars: absorption lines – galaxies: evolution – galaxies: high redshift – galaxies: ISM – galaxies: star formation.

## 1. Introduction

The diffuse interstellar medium (ISM) exhibits a wide range of physical conditions such as temperature, density and radiation field, and structures at tens of AU to kpc scales in the form of shells, filaments and spurs. The conditions in the ISM are intimately related to the local star-formation through various stellar feedback mechanisms. Therefore understanding the physical conditions and the structure of gas in the ISM, and the processes that maintain these is a key topic in the field of galaxy evolution. The absorption lines seen in the spectra of distant luminous sources such as quasi-stellar objects (QSOs) and Gamma-ray bursts (GRBs) provide a powerful tool to determine the physical and chemical state of the different phases of ISM in both the Galaxy and external galaxies. These absorbers provide a luminosity unbiased view of the galaxy evolution and measurements of the physical parameters of gas at the scales much smaller than that possible with the continuum and emission line studies.

Due to their observability with the ground based optical telescopes, the resonant absorption lines of Mg II are commonly used for detecting the interstellar media and/or gaseous halos

surrounding the galaxies at  $z \lesssim 2$ . The availability of large samples of low resolution quasar spectra from the Sloan Digital Sky Survey (SDSS) has led to the compilation of large homogeneous catalogues of Mg II absorbers at  $0.35 < z_{\text{abs}} < 2.3$  that are complete down to  $W_r(\text{Mg II } \lambda 2796) = 1 \text{ \AA}$  (see e.g., Prochter et al. 2006; Quider et al. 2011). It has been shown using the Hubble Space Telescope (HST) spectroscopic observations that a significant fraction ( $36\% \pm 6\%$ ) of Mg II systems with the rest equivalent widths<sup>1</sup>,  $W_r > 0.5 \text{ \AA}$  and  $W_r(\text{Fe II } \lambda 2600) > 0.5 \text{ \AA}$  have  $N(\text{H I}) \geq 2 \times 10^{20} \text{ cm}^{-2}$  and therefore are bonafide damped Ly $\alpha$  (DLA) systems (Rao et al. 2006). The optical imaging and spectroscopic surveys have shown that the Mg II absorbers are associated with the galaxies of a wide range of morphological type and are routinely observed out to galactic radii of  $\sim 50 \text{ kpc}$ . (e.g. Bergeron & Boissé 1991; Steidel 1995; Churchill et al. 2005; Chen et al. 2010a; Rao et al. 2011; Bowen & Chelouche 2011).

While it is well established that the Mg II absorption lines arise from the gas associated with the galaxies, the exact nature and the underlying physical process driving the gas seen

<sup>1</sup> Throughout this paper,  $W_r \equiv W_r(\text{Mg II } \lambda 2796)$  unless specified.

in absorption is still a matter of debate. Using the integral field spectroscopy, Bouché et al. (2007) have detected H $\alpha$  emission associated with the 14 intervening Mg II absorbers ( $W_r > 2 \text{ \AA}$ ) within the QSO impact parameters of 1-40 kpc implying large star formation rates (SFRs) of  $1\text{--}20 M_\odot \text{ yr}^{-1}$ . Similarly, the [O II] emission lines corresponding to the absorbing galaxies have been detected in the individual as well as the stacked QSO spectra of  $W_r > 0.7 \text{ \AA}$  Mg II absorbers (Noterdaeme et al. 2010b; Ménard et al. 2011). These results point towards a strong physical connection between the starburst phenomena and the absorbing gas associated with the strong ( $W_r \gtrsim 1 \text{ \AA}$ ) Mg II absorbers (see also Prochter et al. 2006; Murphy et al. 2007; Nestor et al. 2011). On the other hand, the weaker Mg II absorbers are believed to be tracing the infalling/accreting gas (Chen et al. 2010b; Kacprzak & Churchill 2011).

The detection of 21-cm absorption in a well defined sample of Mg II absorbers towards the radio-loud quasars can be used to estimate the filling factor of cold gas in Mg II systems. Until blind surveys of radio absorption lines become a real possibility, this is also the only practical way to search for the 21-cm absorption at  $0.2 < z_{\text{abs}} < 2$  and trace the evolution of cold gas in galaxies. Since the cold neutral medium (CNM) filling factor of gas depends sensitively on the stellar feedback, such surveys can also provide insights into the physical processes driving the gas seen in Mg II absorption. There have been several searches for 21-cm absorption in Mg II systems (e.g. Briggs & Wolfe 1983; Lane 2000; Curran et al. 2007; Kanekar et al. 2009). A systematic survey of 21-cm absorption in a sample of 35 intervening Mg II absorbers at  $1.1 < z_{\text{abs}} < 1.5$  was presented in Gupta et al. (2007) and Gupta et al. (2009, hereafter referred to as G09). The detection of 9 new 21-cm absorbers from this survey significantly increased the number of known 21-cm absorbers at the intermediate redshifts.

G09 provided first estimate of the number density per unit redshift of 21-cm absorbers ( $n_{21}$ ) associated with the  $W_r \geq 1 \text{ \AA}$  Mg II absorbers. Hereafter, we will refer to  $W_r \geq 1 \text{ \AA}$  absorbers as the *strong* Mg II absorbers. Using the twenty-one 21-cm absorption measurements at  $0.3 < z_{\text{abs}} < 1$  from the sample of Lane (2000), they showed that the  $n_{21}$  at  $z = 1.3$  may have decreased with respect to the  $n_{21}$  at  $z = 0.5$ . The evolution was found to be stronger for the stronger ( $W_r \geq 1.8 \text{ \AA}$ ) Mg II systems. This could be due to the evolution of the CNM filling factor of the gas in galaxies, and the fact that the stronger Mg II systems at higher- $z$  possibly arise in the outflows driven by starbursts (Prochter et al. 2006; Noterdaeme et al. 2012). This interpretation of the results from the survey was limited by the availability of the milliarc-second scale radio images of the background quasars and the lack of sensitive 21-cm absorption measurements at  $z < 1$ .

As an extension of our work presented in G09, we present here the new 21-cm absorption measurements of the 17 Mg II systems at  $0.5 < z_{\text{abs}} < 1.5$  and the 20-cm Very Long Baseline Array (VLBA) maps of the 40 quasars to study the evolution of CNM filling factor of Mg II systems and investigate the effect of radio source structure on the detectability of 21-cm absorption. The 21-cm absorption measurements were made using the Green Bank Telescope (GBT), the Giant Metrewave Radio Telescope (GMRT) and the Westerbork Synthesis Radio Telescope (WSRT). The details of these 21-cm absorption and the VLBA observations, and the new 21-cm absorption detections are provided in Section 2. In Section 3, we describe the assumptions and method used to determine the correction for partial coverage using the milliarcsecond scale VLBA maps. We define a homogeneous sample that is selected primarily on the

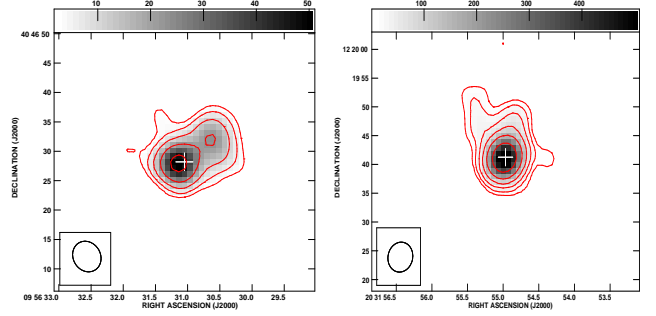


**Fig. 1.** GMRT maps of J0956+4046 (*left*) and J2031+1219 that are resolved in our observations at  $\sim 610$  MHz with contour levels as  $n \times (-1, 1, 2, 4, \dots)$  mJy beam $^{-1}$ , where  $n=2.8$  and 10 respectively. The maps have rms of 0.36 and 1.4 mJy beam $^{-1}$ , and the beams are  $5.43'' \times 4.76''$  (position angle PA= $37^\circ$ ), and  $5.34'' \times 4.96''$  (PA= $-39^\circ$ ) respectively. The position of the optical source is marked as ‘+’ (SDSS for J0956+4046; Condon et al. 1977, for J2031+1219).

basis of  $W_r \geq 1 \text{ \AA}$  criterion. This sample is used to derive the 21-cm detection rate in strong Mg II absorbers as a function of redshift. In Section 4, we discuss the relationship between the 21-cm absorption and the radio structure of the background quasar. The relationship of 21-cm absorption with the properties of metal absorption lines and the dust content of the absorbing gas derived from the optical spectra are discussed in Section 5. We discuss the implications of our results in Section 6. The results are summarised in Section 7.

Throughout this paper we use the  $\Lambda$ CDM cosmology with  $\Omega_m=0.27$ ,  $\Omega_\Lambda=0.73$  and  $H_0=71 \text{ km s}^{-1} \text{ Mpc}^{-1}$ .

## 2. Data

### 2.1. Redshifted 21-cm line observations

#### 2.1.1. Sample

Our sample of Mg II absorbers to search for 21-cm absorption is listed in Table 1. The sample is mostly drawn from the SDSS Data Release 7 using an automatic procedure that fits the QSO continuum redwards of the Ly $\alpha$  emission using Savitzky-Golay filtering and identifies Mg II doublets at  $0.35 < z_{\text{abs}} < 2.3$  through a correlation analysis. Similar to G09, we confine our sample to the Mg II systems with  $W_r \geq 1 \text{ \AA}$ . The sample was designed for observations with the GMRT 610-MHz and WSRT UHF-high receivers (see Section 2.1.2). Therefore we selected Mg II systems at  $0.5 < z_{\text{abs}} < 1.0$  and  $1.1 < z_{\text{abs}} < 1.5$ . Although Mg II systems down to the redshifts of  $\sim 0.35$  can be detected in the SDSS spectra and the corresponding redshifted 21-cm absorption is observable with the WSRT UHF-high receiver, we chose the lower redshift cut-off of our sample to be at  $z_{\text{abs}}=0.5$  to avoid the frequencies around 950 MHz that are known to be affected by strong radio frequency interference (RFI). By cross correlating the position of the QSOs having strong intervening Mg II absorption with radio sources in the Faint Images of the Radio Sky at Twenty-Centimeters (FIRST) catalogue we identified Mg II systems that are in front of the quasars brighter than 100 mJy at 20-cm. After visual inspection of the optical spectra and radio images to ensure that there are no false identifications, we selected 19 Mg II systems that are not covered in G09 for our observations.

In addition, we selected 4 strong Mg II systems towards well known blazars with the metal absorption line prop-

**Table 1.** The sample of strong Mg II systems ( $W_r(\text{Mg II } \lambda 2796) \geq 1 \text{ \AA}$ ) observed with the GBT, GMRT and WSRT. The systems for which no useful 21-cm absorption spectra could be obtained are also given. Listed from left to right are the names of the quasars, their emission redshifts, redshifts of the intervening Mg II system, rest frame equivalent widths of the Mg II  $\lambda 2796$ , Mg II  $\lambda 2803$ , Mg II  $\lambda 2852$  and Fe II  $\lambda 2600$  absorption lines, and 1.4 GHz peak flux densities of the quasars as determined from the FIRST or NVSS surveys. The last column specifies whether the quasar is compact (C) or resolved (R) at the FIRST resolution. The quasars with the deconvolved sizes  $\leq 2''$  are classified as compact (White et al. 1997).

Quasar	$z_{\text{em}}$	$z_{\text{abs}}$	$W_r(\text{Mg II } \lambda 2796)$ ( $\text{\AA}$ )	$W_r(\text{Mg II } \lambda 2803)$ ( $\text{\AA}$ )	$W_r(\text{Mg II } \lambda 2852)$ ( $\text{\AA}$ )	$W_r(\text{Fe II } \lambda 2600)$ ( $\text{\AA}$ )	Flux (mJy/beam)	Mor.
<b>Systems with 21-cm absorption spectra</b>								
J045703–232452	1.003	0.8922	2.20±0.02	1.90±0.02	0.61±0.02	1.87±0.02	1640	C <sup>†</sup>
J080036+501044	1.615	1.4146	1.94±0.04	1.70±0.04	0.45±0.05	1.26±0.05	113.9	C
J081710+235223	1.732	1.3060	1.70±0.13	1.53±0.13	0.80±0.15	1.38±0.17	210.4	C
J093035+464408	2.033	0.6216	3.18±0.14	2.87±0.14	1.21±0.14	2.44±0.13	313.9	C
J095631+404628	1.510	1.3237	5.02±0.37	4.19±0.35	2.43±0.36	1.97±0.57	30.6	R
J100718+225126	2.308	0.5602	1.19±0.32	1.89±0.24	0.64±0.27	1.03±0.19	341.3	C
J114856+525425	1.632	0.8306	2.77±0.04	2.39±0.05	0.76±0.06	1.66±0.05	95.6	C
J121604+584333	1.454	0.7487	1.55±0.12	1.44±0.12	0.47±0.12	0.97±0.11	376.8	R
J125227+442737	1.347	0.9112	1.39±0.15	1.33±0.14	0.36±0.13	1.24±0.14	248.7	R
J132901+105304	1.933	0.6715	1.47±0.18	1.45±0.18	<0.24	1.00±0.25	111.2	C?
J133335+164903	2.089	0.7448	1.80±0.04	1.46±0.04	0.18±0.04	0.53±0.05	409.1	C
J140856–075227	1.500	1.2753	2.08±0.05	1.90±0.05	0.62±0.05	1.53±0.05	604.0	C
J141030+614136	2.247	0.7596	1.31±0.16	1.48±0.16	0.57±0.10	0.84±0.19	116.1	C
J150124+561949	1.467	1.2788	1.38±0.10	1.02±0.09	0.37±0.10	0.72±0.12	148.8	C
J163638+211255	1.801	0.8000	2.26±0.20	2.41±0.21	0.53±0.24	1.62±0.20	365.8	C
J203155+121941	1.215	1.1158	1.29±0.05	1.16±0.05	0.54±0.05	1.12±0.05	941.0	R <sup>†</sup>
J212912–153841	3.268	0.6628	2.49±0.003	–	–	–	589.7	R <sup>†</sup>
<b>Systems with VLBA image but no 21-cm absorption spectra</b>								
J081534+330529	2.426	0.8515	2.67±0.28	2.19±0.31	0.55±0.15	1.12±0.27	327.9	C
J110021+162914	3.380	0.8540	1.99±0.11	1.64±0.11	0.66±0.12	1.08±0.13	256.5	C
J115734+163859	1.061	0.7624	1.19±0.07	1.05±0.07	0.25±0.08	0.56±0.07	734.3	C
J121332+130720	1.139	0.7718	1.19±0.08	1.10±0.08	0.36±0.09	0.81±0.08	1281.0	C
J130036+082802	1.090	0.8665	1.39±0.08	1.07±0.08	0.48±0.10	0.78±0.11	101.3	C
J143009+104326	1.710	1.2431	1.64±0.09	1.53±0.09	<0.10	0.64±0.17	303.9	C

**Notes.** <sup>(†)</sup> Not covered in FIRST. The flux densities for J0457–2324, J2031+1219 and J2129–1538 are taken from the NVSS. The morphology classification for J0457–2324 and J2129–1538 is based on the 1.4 GHz VLA images with the resolution of  $\sim 3''$  and  $\sim 1.4''$  respectively (Ulvestad et al. 1981; Neff & Hutchings 1990). More than 90% of the flux density of J0457–2324 is contained in an unresolved component whereas J2129–1538 exhibits a core-jet morphology with linear size of  $4.6''$  and 95% of the total flux density in the core component. The quasar J2031+1219 is extended in the GMRT image at 610 MHz (resolution  $\sim 5''$ ) presented in Fig. 1.

erties suggesting a high probability of them being DLAs. The  $z_{\text{abs}} = 0.8922$  system towards the BL Lac J0457–2324 (PKS 0454–234), the  $z_{\text{abs}} = 1.2753$  system towards the FSRQ J1408–0752 (PKS 1406–076), and the  $z_{\text{abs}} = 1.1158$  system towards the BL Lac J2031+1219 (PKS 2029+121), were selected from the sample of Mg II systems towards blazars given in Bergeron et al. (2011). The  $z_{\text{abs}} = 0.6628$  system towards the FSRQ J2129–1538 (PKS 2126–158) was identified in the UVES/VLT large programme data (Bergeron et al. 2004).

In total, we have a sample of 23 strong Mg II systems. The rest equivalent widths of Mg II  $\lambda 2852$ , Mg II  $\lambda 2796$ , Mg II  $\lambda 2803$  and Fe II  $\lambda 2600$  for these are given in the Table 1. The equivalent widths have been estimated by integrating over the absorption profile as done in G09. The Mg II  $\lambda 2852$ , Mg II  $\lambda 2803$ , and Fe II  $\lambda 2600$  absorption lines for the system towards J2129–1538 fall in the Ly $\alpha$  forest, and their profiles are blended with the other absorption features. For this reason, the equivalent widths for these absorption lines for this system are not given in Table 1. A detailed analysis of this system will be presented in Boissé et al. (in prep.).

## 2.1.2. Observations and data reduction

The systems at  $0.5 < z_{\text{abs}} < 1.0$  were observed using the WSRT UHF-high receiver whereas the systems at  $1.1 < z_{\text{abs}} < 1.5$  were observed using the GMRT 610-MHz receiver. The latter corresponds to the frequency coverage of the 610-MHz receiver. The systems at  $z_{\text{abs}} < 1$  that could not be observed with the WSRT or resulted in the spectra severely affected by the RFI were subsequently observed with the GBT prime-focus PF1-800 MHz receiver. In total, we observed 17 systems from our sample. The Observing log is provided in Table A.1. For the GBT observations of 9 Mg II systems, we used the Spectral Processor as the backend with a bandwidth of 2.5 MHz split into 1024 spectral channels. In addition, fast time sampling of 1 sec was used. The observations were done in standard position-switching mode with typically 5 min spent on-source and same amount of time spent at the off-source position. The data were acquired in two linear polarization channels i.e. XX and YY. The GMRT and WSRT observations were done using baseband bandwidth of 1 MHz split into 128 and 2.5 MHz split into 1024 frequency channels respectively. For flux density and bandpass calibration, the standard flux density calibrators such as 3C48, 3C147 and 3C286 were observed. In GMRT observations, a phase calibra-

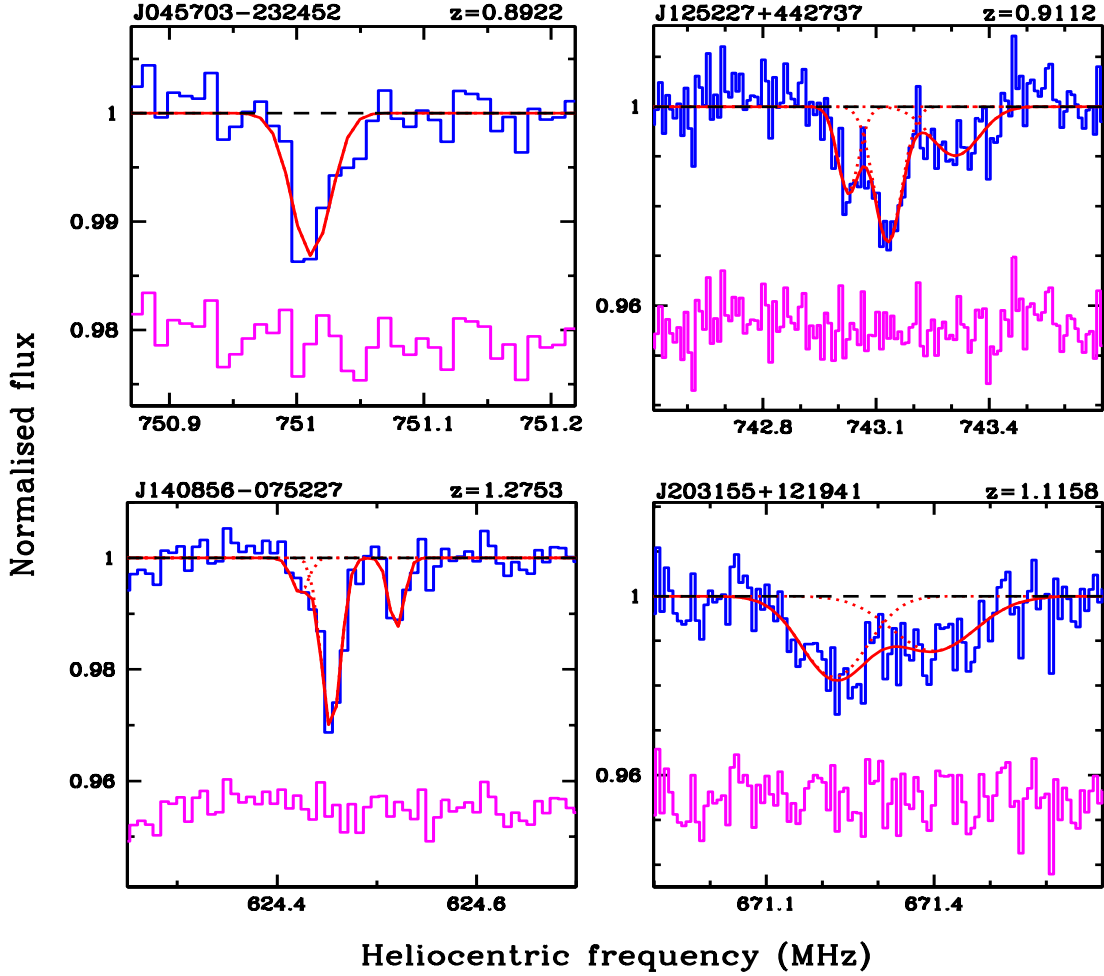


**Fig. 2.** Spectra of 21-cm absorption detections from the GBT (*top*) and GMRT (*bottom*). Individual Gaussian components and resultant fits to the absorption profiles are overplotted as dotted and continuous lines respectively. Residuals, with an arbitrary flux offset for clarity, are also shown.

tor was also observed for 10 min after every  $\sim 45$  min to get reliable phase solutions. The data were acquired in the two polarization channels RR and LL. The total on-source time after excluding telescope set-up time and calibration overheads are also provided in Table A.1.

The GMRT and WSRT data were reduced using NRAO Astronomical Image Processing System (AIPS) following the standard procedures as described in Gupta et al. (2006). Unfortunately, the WSRT data for the systems towards J1007+2251, J1148+5254, J1216+5843 and J1329+1053 were severely affected by RFI. Although no useful spectrum could be obtained for these systems, the data were still useful for measuring the flux densities of J1007+2251, J1216+5843 and J1329+1053 at the redshifted 21-cm frequencies, and estimating the accurate optical depths from the GBT data. The GMRT and WSRT observations resulted in 2 new 21-cm absorption detections and 21-cm optical depth limits for 6 systems. The continuum images of two quasars that are resolved in the GMRT observations are presented in Fig. 1. The quasar J0956+4046 is resolved into two peaks. We refer to the southern component which is coincident with the optical QSO as P1 and the other component as P2 in the following text.

We used NRAO’s GBTIDL package to develop a pipeline to automatically analyse the GBT spectral-line datasets. After excluding the time ranges for which no useful data were obtained, the data were processed through this pipeline. The pipeline calibrates each data record individually and flags the spectral channels with deviations larger than  $5\sigma$  seen in either XX or YY as affected by RFI. After subtracting a first order baseline these data are averaged to produce the baseline (i.e. continuum) subtracted spectra for XX and YY. The baseline fit and statistics for flagging are determined using the spectral region that excludes central 25% and last 10% channels at both ends of the spectrum. If necessary a first-order cubic spline was fitted to the averaged XX and YY spectra obtained from the pipeline, which were then combined to produce the stokes I spectrum. The spectrum was then shifted to the heliocentric frame. The multiple-epoch spectra for a system were then resampled onto the same frequency scale and combined to produce the final spectrum. These GBT observations resulted in 2 new 21-cm absorption detections and 21-cm optical depth limits for 7 systems.

The confusion due to other radio sources in the primary beam is not an obstacle in determining accurate flux densities of the background quasars and optical depths for the systems observed with the GMRT and WSRT. But for the systems observed with

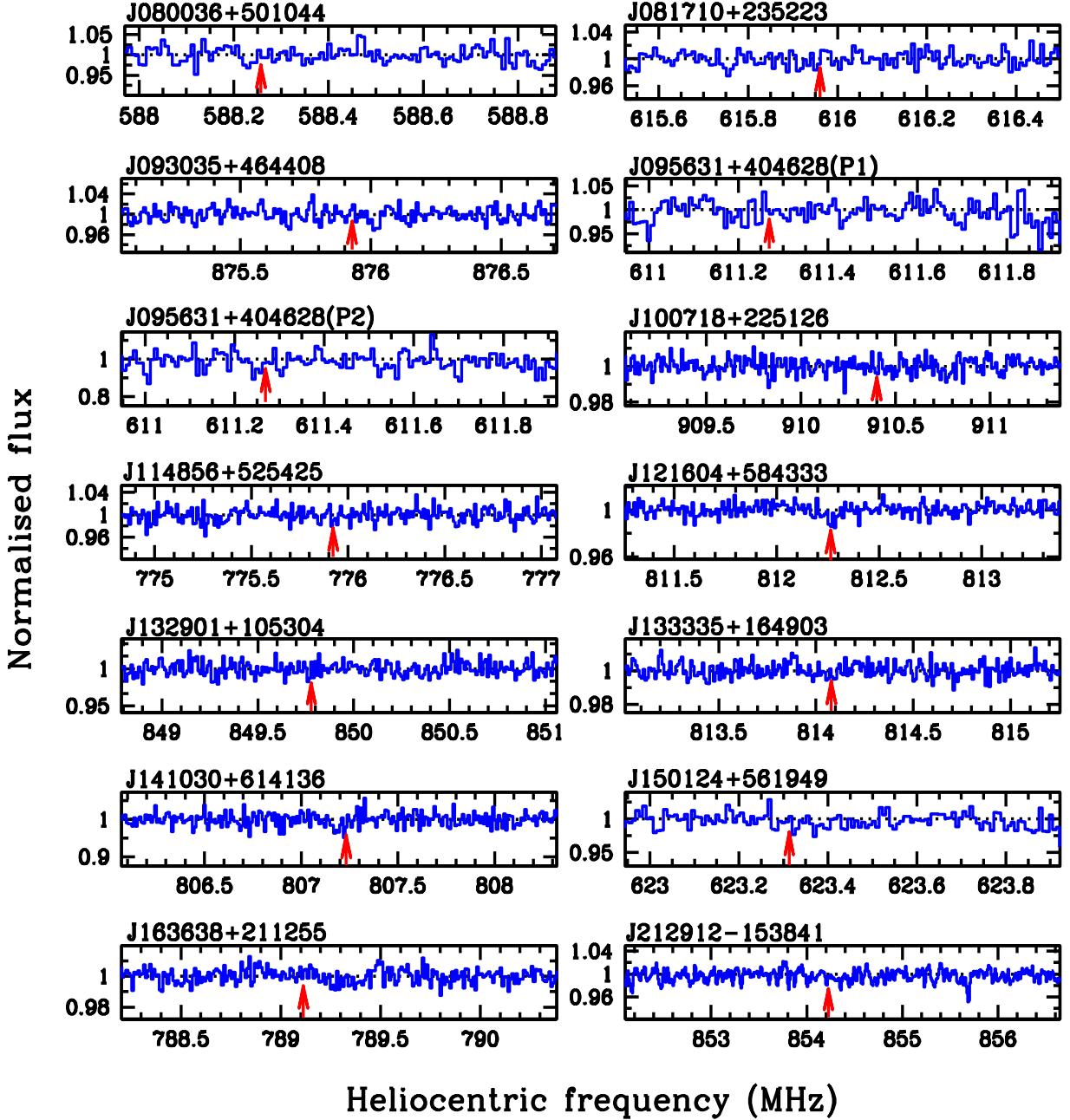


**Fig. 3.** GBT, GMRT and WSRT spectra of the Mg II systems with 21-cm non-detection. Arrows mark the expected positions of 21-cm absorption lines based on metal absorption lines. For J0956+4046, P1 and P2 correspond to spectra towards the southern and the northern peaks respectively (see Fig. 1 and the text for details).

the GBT, the rms confusion due to other sources in the beam can be the dominant effect that limits the accuracy with which the 21-cm optical depth can be determined. We used interferometric images from our WSRT observations and literature to address this issue. The details are provided in Appendix B and the flux densities and optical depth values for all the systems are listed in Table B.1.

In summary, our spectroscopic observations have resulted in 4 new 21-cm absorption detections that are shown in Fig. 2. The spectra of 13 21-cm non-detections are presented in Fig. 3. The GMRT spectra are at a spectral resolution of  $\sim 4 \text{ km s}^{-1}$  whereas GBT and WSRT spectra have been smoothed to  $\sim 4 \text{ km s}^{-1}$ . For

the exact resolution of the spectra plotted in Figs. 2 and 3 see Table B.1.

## 2.2. Details of new 21-cm absorption detections

Now we present the details of 4 new 21-cm absorption detections (Fig. 2). In Table 2 we provide the details of Gaussian components i.e. the absorption redshift ( $z_{\text{abs}}$ ), the full width at half maximum (FWHM) and the peak optical depth ( $\tau_p$ ) fitted to these spectra. These Gaussian components provide convenient parametrization of absorption lines even if they do not necessarily represent the actual physical components.

**Table 2.** Details of multiple Gaussian fits to 21-cm absorption profiles. Listed from left to right are the names of quasars, and the absorption redshifts, FWHMs and peak optical depths of the Gaussian components.

Quasar	$z_{\text{abs}}$	FWHM ( $\text{km s}^{-1}$ )	$\tau_p$
J0457–2324	0.89132	$14 \pm 2$	$0.013 \pm 0.002$
J1252+4427	0.91138	$35 \pm 6$	$0.027 \pm 0.002$
	0.91092	$61 \pm 16$	$0.010 \pm 0.002$
	0.91165	$27 \pm 6$	$0.017 \pm 0.003$
J1408–0752 <sup>†</sup>	1.27464	$11 \pm 1$	$0.031 \pm 0.002$
	1.27440	$9 \pm 2$	$0.013 \pm 0.002$
	1.27475	$10 \pm 6$	$0.006 \pm 0.002$
J2031+1219	1.11558	$78 \pm 24$	$0.013 \pm 0.002$
	1.11614	$62 \pm 12$	$0.018 \pm 0.002$

**Notes.** <sup>(†)</sup> Corresponds to the spectrum taken on 21/6/2009 (see Fig. 2).

- $z_{\text{abs}}=0.8922$  system towards J0457–2324: The background quasar, also known as PKS0454–234, is a BL Lac object and highly polarized with optical polarization of 27% (Wills et al. 1992). The 21-cm absorption detected in our GBT spectrum has velocity width,<sup>2</sup>  $\Delta V=23.4 \text{ km s}^{-1}$  and integrated 21-cm optical depth,  $\int \tau dv=0.20 \pm 0.02 \text{ km s}^{-1}$ . The H I column density of an optically thin cloud covering the fraction  $f_c$  of the background radio source is related to the integrated 21-cm optical depth and the spin temperature ( $T_s$ ) through

$$N(\text{H I}) = 1.823 \times 10^{18} \frac{T_s}{f_c} \int \tau(v) dv \text{ cm}^{-2}. \quad (1)$$

This corresponds to an H I column density of  $N(\text{H I})=5.8 \times 10^{19} (T_s/100)(0.63/f_c) \text{ cm}^{-2}$  for the absorber towards J0457–2324. Here, we have assumed  $f_c = c_f$  where  $c_f$  is defined as the ratio of the flux density of the VLBA ‘core’ to the total arcsecond scale flux density (see Section 3 for the details regarding  $f_c$ ).

- $z_{\text{abs}}=0.9112$  system towards J1252+4427: The background quasar is resolved in FIRST survey with a deconvolved size of  $3.68'' \times 1.01''$ . The 21-cm absorption detected in our GBT spectrum has  $\Delta V=134 \text{ km s}^{-1}$  and  $\int \tau dv=2.06 \pm 0.13 \text{ km s}^{-1}$ . This corresponds to  $N(\text{H I})=3.8 \times 10^{20} (T_s/100)(1/f_c) \text{ cm}^{-2}$ . No subarcsecond scale images are available for this quasar to constrain  $f_c$ .
- $z_{\text{abs}}=1.2753$  system towards J1408–0755: The background quasar is a blazar at  $z=1.494$  and the associated radio jet at milliarcsecond scale exhibits the highest superluminal velocity ( $>25c$ ) amongst the known blazars (Piner et al. 2006). The 21-cm absorption detected in our GMRT spectrum has  $\Delta V=45.0 \text{ km s}^{-1}$  and  $\int \tau dv=0.51 \pm 0.05 \text{ km s}^{-1}$ . This corresponds to  $N(\text{H I})=2.5 \times 10^{20} (T_s/100)(0.38/f_c) \text{ cm}^{-2}$ , where we have assumed  $f_c = c_f$ . We reobserved this system with the GMRT after 7 months (Table A.1) to obtain the higher resolution spectrum and investigate the variability in the 21-cm absorption profile due to jet proper motion. This higher resolution spectrum is presented in the top panel of Fig. 4. It shows three well detached components: A1, A2 and A3.

<sup>2</sup> Velocity width of absorption profile corresponding to the 5% and 95% percentiles of the apparent optical depth distribution estimated using the method described by Ledoux et al. (2006).

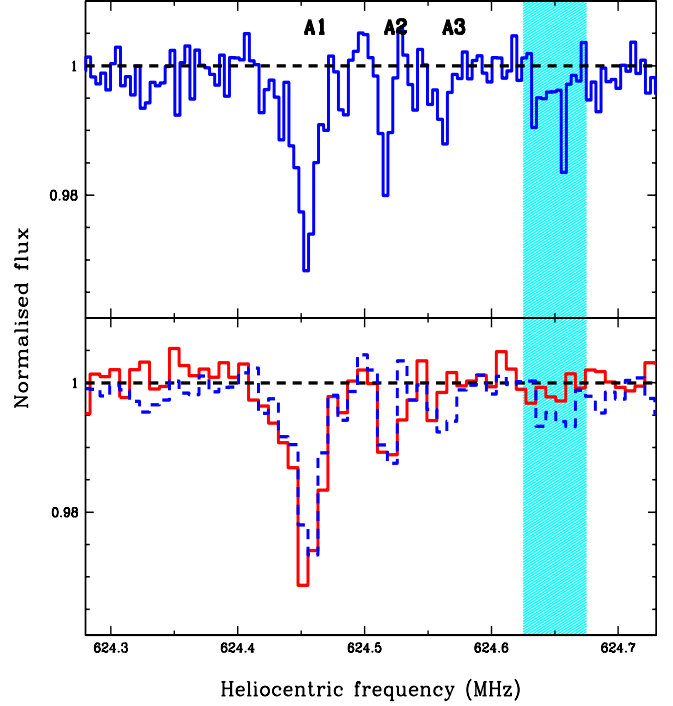


**Fig. 4.** 21-cm absorption spectra of  $z_{\text{abs}}=1.2753$  Mg II absorber towards J1408–0752. Top panel shows the higher resolution ( $1.9 \text{ km s}^{-1}$ ) spectrum taken on 22/1/2010 and bottom panel shows the lower resolution ( $3.8 \text{ km s}^{-1}$ ) spectrum taken on 21/6/2009. The 22/1/2010 spectrum smoothed to the resolution of 21/6/2009 spectrum is also plotted (dashed line) in the bottom panel. The shaded region corresponds to the RFI affected spectral range in the higher resolution spectrum.

The detection of multiple components in this absorber could be related to the complex morphology exhibited by this radio source at milliarcsecond scales. While the components A1 and A2 are clearly detected at both the epochs, the same cannot be said about the component A3. The component A3 has  $\int \tau dv=0.07 \pm 0.02 \text{ km s}^{-1}$  and is detected with a significance of  $3.7\sigma$  at the second epoch. Unlike the features in the RFI affected spectral range shown in Fig. 4, the component A3 is also consistently reproduced in the spectra from the two polarisations. However, due to the lower resolution and S/N we cannot be certain of the presence of this component at the first epoch. If this component is indeed real and was not present at the first epoch then it would be related to the small scale structure in the CNM gas being traced by the jet components (e.g. C2, C3 or C4 as defined by Piner et al. 2006). The proper motion of  $\sim 0.3 \text{ mas yr}^{-1}$  as measured by Piner et al. (2006) for these components would correspond to a scale of  $\sim 2 \text{ pc}$  at the absorber redshift for a period of seven months. The follow-up GMRT observations to investigate this further are in progress.

- $z_{\text{abs}}=1.1158$  system towards J2031+1219: The background radio source is a BL Lac object at  $z=1.215$ . This radio source is extended in our GMRT image (Fig. 1). The VLA A-array map from Rector & Stocke (2001) shows this quasar to be core dominated at the arcsecond scales. A broad and shallow 21-cm absorption is detected towards this quasar. The 21-cm absorption detected in our GMRT spectrum has

$\Delta V = 143 \text{ km s}^{-1}$  and  $\int \tau dv = 2.11 \pm 0.15 \text{ km s}^{-1}$ . This corresponds to  $N(\text{H I}) = 8.6 \times 10^{20} (T_s/100) (0.45/f_c) \text{ cm}^{-2}$ , where we have assumed  $f_c = c_f$ .

### 2.3. Defining a homogeneous sample of 21-cm absorbers: measurements from literature

The purpose of this Section is to define a sample that includes only the 21-cm absorption measurements of the Mg II systems that have been primarily selected on the basis of  $W_r \geq 1 \text{ \AA}$  criterion, and is therefore suitable for determining the 21-cm detection rate in the strong Mg II systems and its redshift evolution in an unbiased way. Hereafter, we refer to this homogeneous sample as S1. From our survey presented in this paper and G09, in total, we have 21-cm absorption measurements for 50 strong Mg II systems over the redshift range  $0.5 < z < 1.5$  albeit with a small gap at  $z \sim 1$ . The redshift distribution of these systems is plotted in the Fig. 5. Only 46 of these systems that are selected primarily on the basis of  $W_r \geq 1 \text{ \AA}$  Mg II absorption should be included in the sample S1. We do not include 4 systems towards the blazars mentioned in Section 2.1.1 in S1 as these were specifically selected on the basis of metal absorption line properties suggesting the H I column densities similar to the DLAs (see Section 5.1). It is probably not just a coincidence that 3 of these systems are detected in the 21-cm absorption (Section 2.2).

Next we enlarge the sample S1 by considering those 21-cm absorption measurements from the literature that match our sample definition i.e. (1) fall in the redshift range:  $0.5 < z < 1.0$  and  $1.1 < z < 1.5$ , and (2) selected primarily on the basis of  $W_r \geq 1 \text{ \AA}$  criterion. Since the inclusion of individually reported detections from the literature can bias our detection rate estimates, we take measurements only from the Mg II selected samples of Lane (2000) and Kanekar et al. (2009) for which both the 21-cm detections and non-detections have been systematically reported. From Kanekar et al. (2009), the independent measurements for 4 systems at  $1.1 < z < 1.5$  and 18 systems at  $0.5 < z < 1.0$  are available. These are listed in Table C.1. We have measured metal absorption line equivalent widths for these systems from the SDSS and the VLT archival spectra by integrating over the absorption profile in the same way as for our systems. Measurements for 13  $W_r \geq 1 \text{ \AA}$  systems at  $0.5 < z < 1.0$  are available from Lane (2000). These are listed in Table D.1.

Thus, we have a homogeneous sample S1 of 81 strong Mg II systems with 21-cm absorption measurements. This sample having 12 21-cm detections will be used for investigating the redshift evolution of 21-cm detection rate amongst the Mg II absorbers. The full sample, hereafter referred as S2, of 85 systems that also includes 4 above mentioned systems towards the blazars will be used when examining the relationship of 21-cm absorption line properties with the radio structure and metal absorption line ratios. A summary of these samples is provided in Table 3. In Fig. 5, we plot 21-cm optical depths as a function of redshift for the sample S2. For uniformity and ease of comparison with the measurements from literature, the 21-cm optical depth limits ( $\int \tau_{3\sigma} dv$ ) for all the systems have been computed for a velocity resolution of  $10 \text{ km s}^{-1}$ . The median  $\int \tau_{3\sigma} dv$  achieved for the systems from Lane (2000) is  $\sim 0.64 \text{ km s}^{-1}$ . This is at least a factor three lower sensitivity as compared to that achieved for our measurements or for the systems from Kanekar et al. (2009). The method we use to estimate the 21-cm detection rates by taking into account the variation in opti-

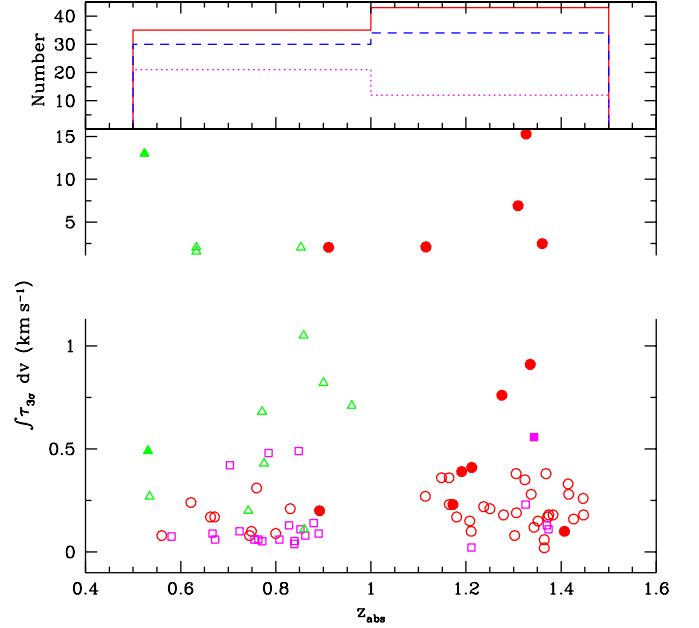


**Fig. 5.** Redshift distribution of 21-cm optical depths for the strong Mg II absorbers from this paper and G09 (circles), Kanekar et al. (2009) (squares) and Lane (2000) (triangles). The filled symbols are for 21-cm absorption detections and the open symbols correspond to  $3\sigma$  optical depth limits for 21-cm non-detections. In the *top* panel, dotted, dashed and solid line histograms are for the sample S2 with  $\int \tau_{3\sigma} dv \leq 0.1, 0.3$  and  $0.5 \text{ km s}^{-1}$  respectively.

cal depth sensitivities towards different quasar sight lines is described in Section 3.1.

## 2.4. VLBA continuum observations

### 2.4.1. Motivation and sample

The detectability of 21-cm absorption, in addition to the optical depth, depends directly on the covering factor,  $f_c$ , of the absorbing gas (see Equation 1). Since radio sources in general exhibit emission over a wide range of physical scales ranging from pc to kpc the  $f_c$  will depend both on the overall extent of the background quasar and the small-scale structure (i.e. clumpiness) of absorbing gas. The motivation behind these VLBA observations is to understand the relationship between the detectability of 21-cm absorption and the structure in the radio source and absorbing gas at the scales of tens of pc. For this purpose we selected all the systems from our sample that are towards the quasars compact at arcsecond scales. This list of 42 Mg II systems towards 40 quasars is drawn from Table 1 of G09 and Table 1 of this paper, and it includes all the systems towards the compact quasars from our sample with 21-cm absorption spectra. Exceptions are J0457–2324 and J2031+1219. The former, although compact at arcsecond scales, could not be observed whereas observations of BL Lac J2031+1219, extended at arcsecond scales, could be included within our observing schedule.

**Table 3.** Summary of all the  $W_r \geq 1 \text{ \AA}$  Mg II absorbers at  $0.5 < z < 1$  and  $1.1 < z < 1.5$  with 21-cm absorption measurements considered here. The samples S1 and S2 discussed in the text are comprised of the subsamples B-E and A-E, respectively.

Sample	Number of systems	21-cm absorption detections	Selection criterion	Reference
A	4	3	$W_r \geq 1 \text{ \AA} + \text{Zn II/Cr II/Mn II}$	This paper
B	13	1	$W_r \geq 1 \text{ \AA}$	"
C	32 <sup>†</sup>	8	"	Gupta et al. (2009)
D	23	1	"	Kanekar et al. (2009)
E	13	2	"	Lane (2000)

**Notes.** <sup>(†)</sup> Measurements of 33  $W_r \geq 1 \text{ \AA}$  Mg II systems are available from G09. However, the optical depth value for the system towards J1145+0455 is taken from the more sensitive spectrum of Kanekar et al. (2009).

#### 2.4.2. Observations and data reduction

The VLBA 20-cm observations were done as part of a larger survey to obtain milliarcsecond scale images of the quasars with DLAs and Mg II systems along the sight line. Observations were carried out on 28/10/2008 (~5 hrs), 7/11/2008 (~14 hrs), 21/2/2010 (~11 hrs) and 10/6/2010 (~17 hrs) (Srianand et al. 2012). We used eight 8 MHz baseband channels i.e. the total bandwidth of 64 MHz. Each baseband channel was split into 32 spectral points. Both the right-hand and left-hand circular polarization channels were recorded. Two bit sampling and the time resolution of 2 seconds were used.

The observations were done using nodding-style phase-referencing with a cycle time of ~5 min i.e. ~3 min on the source and ~1.5 min on the phase-referencing calibrator. The phase-referencing calibrators were selected from the VLBA Calibrator Survey (VCS)<sup>3</sup> at 13-cm and 3.6-cm. In order to improve the *uv*-coverage, the total time on each source was split into *snapshots* over a number of different hour angles. Each source was typically observed for a total of ~30 min. Strong fringe finders/ bandpass calibrators such as J0555+3948, J0927+3902, J1800+3848 and J2253+1608 were also observed every ~3 hrs for 4-5 min.

The data were calibrated and imaged using AIPS and DIFMAP in a standard way (e.g. Beasley et al. 2002). The global fringe fitting was performed on the phase-referencing calibrators. The delays, rates and phases estimated from these were transferred to the target source which was then self-calibrated until the final image was obtained. The VLBA maps of these 40 quasars are presented in Fig. E.1.

The milliarcsecond scale structure was characterised by fitting Gaussian models to the self-calibrated visibilities. The results of the model fitting are provided in columns#5-11 of Table 4. We define  $f_{VLBA}$  as the ratio of total flux density detected in the VLBA and the arcsecond scale image. Similarly,  $c_f$  is defined as the ratio of the flux density of the VLBA ‘core’ component to the total arcsecond scale flux (see Section 3 for details). The largest linear size (LS) represents separation between the farthest components of the radio source at the absorber redshift. For the compact sources represented by single component we take the major axis of the deconvolved component as the upper limit on source size. The  $f_{VLBA}$  and  $c_f$  are discussed in detail in the following sections where we use them to estimate  $f_c$  and correct observed 21-cm optical depths for partial coverage.

#### 2.5. Milliarcsecond scale images from literature and covering factor

The radio morphology of all the quasars in the 21-cm absorption sample S2 are important to our later discussion. Therefore, for the quasars that were not covered in our VLBA 20 cm survey we have compiled this information from literature. For J0457–2324, J1145+0455 and J2129–1538 from our sample, the  $c_f$ ,  $f_{VLBA}$  and largest linear size (LS) obtained using maps at 13-cm from the VCS are provided at the end of Table 4.

In addition, the milliarcsecond images for the 14 quasars with 15 intervening systems taken from Kanekar et al. (2009) are available at 13-cm from the VCS, and for another quasar B0812+332 from our VLBA survey. The  $f_{VLBA}$ ,  $c_f$  and LS for these sources are given in the last three columns of Table C.1.

From the sample of 13 systems taken from Lane (2000), we will consider here only six systems that have been observed with the optical depth sensitivity,  $\int \tau_{3\sigma} dv < 0.6 \text{ km s}^{-1}$ . From this, the milliarcsecond images at 13-cm are available for B0235+164, B0454+039 and B1218+339 from VCS, and for B1629+139 from Dallacasa et al. (1998) (Table D.1). As we shall see later in the Section 4.1, the remaining 7 systems that are all 21-cm non-detections, have been observed with the optical depth sensitivity that is too poor to address the covering factor related issues.

In total, we have information on milliarcsecond scale radio structure for 54 quasars with 57 intervening systems from the sample S2. The VLBA information for the 34 quasars (with 36 systems along their line of sight) are based on 20-cm VLBA images and for the remaining quasars it is based on 13-cm VLBA images. Unlike using the source sizes and flux densities obtained from the Gaussian parametrization of 20-cm maps from our survey, the  $f_{VLBA}$  and  $c_f$  at 13-cm have been estimated using the total and peak flux densities from the VCS. However, these values of the  $c_f$  and  $f_{VLBA}$  for the cases with the ‘core’ identifications, especially in the 13/18 sightlines where the background quasar can be represented by a single component, should not differ<sup>4</sup> by more than ~10% relative to the estimates from the Gaussian parametrization technique. The total arcsecond scale flux densities at 13-cm in all these cases have been estimated by interpolating flux densities available from the NASA extragalactic database. The upper limits on the size of quasars that are represented by single component have been estimated using the major axis of point spread function. These are conservative compared to those obtained using the Gaussian deconvolution.

<sup>3</sup> <http://www.vlba.nrao.edu/astro/calib/>

<sup>4</sup> Based on the data from our 20-cm VLBA survey.



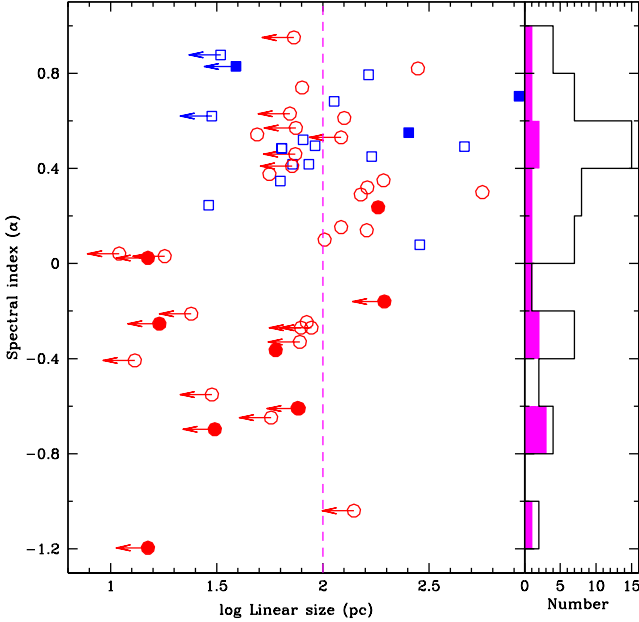


**Fig. 6.** Spectral index ( $\alpha$ ) vs linear size (in pc) at the absorber redshift for the quasars with the milliarcsecond scale images. The  $\alpha$  are from the arcsecond scale images. Systems towards the quasars with no ‘core’ identifications are plotted as squares. The point for the system towards the quasar B1629+120 that has  $\alpha=+0.54$  and LLS=7.2 kpc is not plotted to keep the x-axis short. The histogram for the  $\alpha$  is also shown. The filled symbols and shaded histogram are for 21-cm detections.

### 3. Estimating the gas covering factor and 21-cm absorption detection rate

Radio source structure often consists of a combination of compact components and extended diffuse emission. The latter due to its low surface brightness sensitivity will only contribute to the 21-cm optical depth sensitivity if the large scale structure of the absorbing gas is well aligned to the radio emission of the quasar. Such fortuitous combinations are rare. Therefore by using the flux densities from our spectroscopic observations that at the best have a spatial resolution of  $\sim 30$ –40 kpc at the absorber redshift, in general, we are overestimating optical depth sensitivities.

To show that this is indeed the case with the measurements considered in Table 3, in Fig. 6, we plot the spectral index<sup>5</sup> ( $\alpha$ ) vs linear size (LS) for all the quasars from the sample S2 with milliarcsecond scale images. These spectral indices have been estimated between 20-cm and 50-cm/90-cm using the flux densities from the maps with arcsecond scale resolution and range from  $-1.2$  to  $0.7$ . It is clear from Fig. 6 that the 21-cm detection rate is higher towards the quasars with the flat/inverted spectral indices. The  $44^{+24}_{-16}\%$  (7/16) of systems towards the quasars with  $\alpha \leq 0$  from the sample S2 are detected in 21-cm absorption as compared to the  $15^{+9}_{-6}\%$  (6/41) towards the quasars with  $\alpha > 0$ . It is also clear that 73% of the 21-cm detections are towards the quasars with  $LS \leq 100$  pc and amongst the quasars with  $LS \leq 100$  pc the detection rate is less towards the quasars with steeper spectrum (i.e.  $\alpha > 0$ ). This may imply that the characteristic size of the absorbing gas is less than 100 pc. The low detection rate

in the quasars with the steeper spectrum will then be related to the poor optical depth sensitivity to detect 21-cm absorption towards the ‘cores’. The term ‘core’ is used here to represent the radio component coincident with the optical QSO.

Thus, identifying the ‘core’ component in the sample S2 is important to confirm these suggestions and estimate  $f_c$  of the absorbing gas. For this, we need milliarcsecond scale maps at multiple frequencies to estimate the spectral indices of the various components detected in the 20-cm or 13-cm VLBA maps discussed in Section 2.5. For the 42 systems, images of the background quasar at more than one frequency are available through our observations, the VCS and the VLBA Imaging and Polarization Survey (VIPS). Using these images at 20-cm, 13-cm, 6-cm and 3.6-cm we find that in 36 cases the dominant VLBA component has a flat spectrum at milliarcsecond scales and can be identified as the ‘core’. Although for the quasars J0154–0007, J0845+4257 and J0852+3435 only images at 20-cm are available but all three have more than  $\sim 70\%$  of the arcsecond scale flux contained in the dominant VLBA component. We identify this component as the ‘core’ on the basis of  $\alpha \lesssim 0$  estimated at the arcsecond scale. Therefore, in total, for the 39 systems we identify the dominant VLBA component of the background quasar as ‘core’.

In Fig. 6, we plot 17 quasars with 18 intervening systems that have no ‘core’ identification as squares. In 6 cases, the multifrequency VLBA images are available, but the dominant component at the milliarcsecond scales has a steep spectrum and cannot be identified as ‘core’. No multifrequency VLBA images are available for the remaining 11 quasars with 12 intervening systems. These 17 quasars with no ‘core’ identifications also have on the average steeper spectral index. The  $c_f$  values for these are marked as ‘\*’ in Tables 4 and C.1. This subset of 18 systems includes three 21-cm detections which are towards J1058+4939, J1145+0455 and J1623+0718. The former two exhibit complex morphology at milliarcsecond scales. The third is compact in 20-cm VLBA map but unlike most of the other quasars that are compact at milliarcsecond scales has a low  $c_f$  value of 0.42. We will discuss the nature of these systems in detail in the subsequent sections.

Thus, we have ‘core’ identification for 39 quasars from the sample S2. We will consider the following two scenarios and use  $c_f$  and  $f_{VLBA}$  to estimate  $f_c$  for the 21-cm absorption systems towards these. In the first scenario we define  $f_c = c_f$ . The assumption in this case is that the 21-cm absorbing gas only covers the ‘core’. If the filling factor of the absorbing gas at these scales is unity, this provides a conservative lower limit on the actual value of  $f_c$ . In the second scenario we use  $f_c = f_{VLBA}$ . The assumptions in this case are that the 21-cm absorbing gas extends well beyond  $\sim 300$  pc to cover all the milliarcsecond scale components and the diffuse extended ( $> \text{kpc}$  scale) emission that got resolved out in the VLBA maps does not contribute to the optical depth sensitivity (see also Section 6.3).

#### 3.1. Detection rate

In this Section, we determine 21-cm detection rates in the strong Mg II absorbers. Due to the reasons mentioned in Section 2.3, we will use the homogeneous sample S1 (Table 3) for this purpose. In the sample S1, there are 40 systems at  $0.5 < z < 1$  and 41 at  $1.1 < z < 1.5$ . There are 3 and 9 detections in the low- and high- $z$  bins respectively. The *top* panel of Fig. 5 shows the distribution of optical depth sensitivities in these two redshift bins. We will determine the 21-cm detection rates following the method described in Section 7 of G09 that takes into account the

<sup>5</sup> We adopt the definition that the flux density at frequency  $\nu$ ,  $S_\nu \propto \nu^{-\alpha}$ .

variation of optical depth sensitivities towards different quasar sight lines. The detection rate for 21-cm absorption,  $C$ , (defined as the fraction of Mg II systems that show detectable 21-cm absorption with the integrated optical depths  $\mathcal{T}_{21}$  greater than the  $3\sigma$  limiting value  $\mathcal{T}_0$ ) for the  $0.5 < z < 1$  and  $1.1 < z < 1.5$  bins are given in Table 5. Since the lower limiting values of  $\mathcal{T}_0$  select the weaker 21-cm absorbers and higher values select the stronger absorbers, in Table 5, we give detection rates for a range of  $\mathcal{T}_0$  values suitable for the sample considered here (see the histograms in Fig. 5).

It is clear from Table 5 that the 21-cm detection rate  $C$  for any value of  $\mathcal{T}_0$  is only slightly lower for the low- $z$  bin. Since the number of detections involved are small in both the redshift bins, the errors are large and the noted difference is not statistically significant (i.e. say at more than  $3\sigma$  level). The maximum difference is seen for  $\mathcal{T}_0=0.1 \text{ km s}^{-1}$  and is only significant at the level of  $\sim 0.6\sigma$ . To test this further, we perform the generalized rank correlation test that takes into account the upper limits (Isobe et al. 1986). We find a correlation coefficient of 1.37 and the probability that this correlation occurs by chance of 17%. Therefore the apparent trend is also hinted by the correlation test but once again without high statistical significance.

Thus we conclude that the 21-cm absorption detection rate ‘ $C$ ’ for the strong Mg II absorbers is constant over  $0.5 < z < 1.5$  that is  $\sim 30\%$  of the age of Universe. As the radio emission from quasars originate from a much larger spatial extent than the optical emission, one must pay attention to the issues related to radio source structure. Therefore, before discussing the evolution of ‘ $C$ ’ any further, we investigate the impact of the radio structure of background quasar on the 21-cm detection rate.

#### 4. 21-cm absorption and radio source structure

Curran (2010) has used angular diameter distance ratios ( $DA_{abs}/DA_{qso}$ ) at the absorber and background quasar redshift to investigate the effect of line-of-sight geometry on the coverage of background radio source by the 21-cm absorbing gas. He suggests that since the background radio source can be more effectively covered at the smaller  $DA_{abs}/DA_{qso}$ , the larger values ( $\geq 0.8$ ) of  $DA_{abs}/DA_{qso}$  at  $z_{abs} \geq 1$  can explain the lower 21-cm detection rates at the higher redshifts.

In the homogeneous sample S1, only 4 out of 81 systems have  $0.6 < DA_{abs}/DA_{qso} < 0.8$  and two of these are detected in 21-cm absorption. The remaining 95% of the Mg II systems have  $DA_{abs}/DA_{qso} > 0.8$  and dominate the statistics. As expected, all the 4 systems with  $DA_{abs}/DA_{qso} < 0.8$  are at  $z_{abs} < 1$ . For  $\mathcal{T}_0=0.1 \text{ km s}^{-1}$ , they correspond to  $C=0.50^{+50}_{-32}$ . Interestingly, this is same as the  $C$  for  $\mathcal{T}_0=0.1 \text{ km s}^{-1}$  we obtained in the previous Section for the  $z > 1$  bin with all the systems having  $DA_{abs}/DA_{qso} > 0.8$ . Therefore, we do not see any significant influence of the geometric effects as quantified by Curran (2010) on the detectability of 21-cm absorption in our sample. This also implies that the redshift evolution of 21-cm detection rates over the low- and high- $z$  bins in Table 5 is not affected by any evolution in  $DA_{abs}/DA_{qso}$ .

However, this does not mean that the 21-cm detection rate estimates are not affected by the partial coverage of the background quasar. As discussed in Section 3, the 21-cm optical depth sensitivities from the GBT, GMRT and WSRT observations are overestimated. Our purpose here is to estimate the 21-cm optical depth sensitivities and detection rates corrected for partial coverage. For this we will use  $f_c$  as estimated from the arcsecond and milliarcsecond scale images under reasonable as-

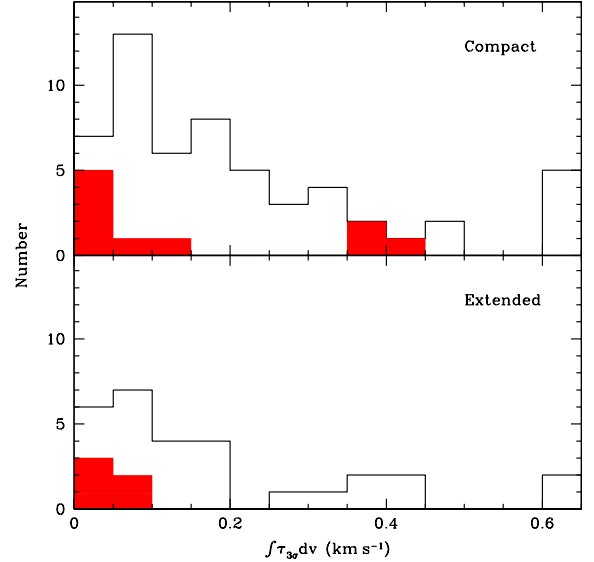


**Fig. 7.** Distribution of 21-cm optical depth sensitivity for the quasars that are compact and extended at arcsecond scales in the sample S2. Shaded histogram shows the sensitivity achieved in case of 21-cm absorption detections. The 7 systems from Lane (2000) with  $\int \tau_{3\sigma} dv > 0.6 \text{ km s}^{-1}$  are placed in the last bin.

sumptions of the gas filling factor and the extent of absorbing gas (cf. Section 3).

##### 4.1. Arcsecond scale radio structure

The sample S2 has 56 and 31 systems towards the quasars that are compact (deconvolved sizes  $< 2''$ ) and extended at arcsecond scales, respectively. The distribution of optical depth sensitivities for these are plotted in Fig. 7. The 21-cm absorption detection rates for  $\mathcal{T}_0=0.3 \text{ km s}^{-1}$  towards the compact and the extended quasars are  $10^{+8}_{-5}\%$  and  $14^{+13}_{-7}\%$  respectively. The detection rates are also similar for  $\mathcal{T}_0=0.1 \text{ km s}^{-1}$  and  $0.5 \text{ km s}^{-1}$ , and do not show any significant difference when the sample is split into the two redshift bins as given in Table 5. However, it is interesting to note from Fig. 7 that while in the case of systems towards the extended quasars the 21-cm absorption is detected only when  $\int \tau_{3\sigma} dv < 0.2 \text{ km s}^{-1}$ , in case of compact quasars the 21-cm absorption is also detected for  $\int \tau_{3\sigma} dv > 0.4 \text{ km s}^{-1}$  (without any correction for the partial coverage). To understand this, we now discuss these detections in detail.

Amongst the systems towards the compact quasars, the three 21-cm detections in the tail of  $\int \tau_{3\sigma} dv$  distribution are towards J0850+5159, J0852+3435 and J2340-0053. The optical depth sensitivities achieved are lower as these systems are towards relatively weaker radio sources in our sample. Still, the 21-cm absorption is detected due to the large 21-cm optical depth. The rare 2175Å UV-bump is detected in the first two cases suggesting the presence of cold gas with a large column density of dust (Srianand et al. 2008; Kulkarni et al. 2011, see also Section 5.2). In the third case, the 21-cm line width is consistent with the absorbing gas having  $T_s < 200 \text{ K}$  resulting in large 21-cm optical depth (G09; Rahmani et al. in prep.).

Now we discuss the 21-cm detections towards the quasars that are extended at arcsecond scales. The 5 detections in this case are towards B0235+164, J0804+3012, J1145+0455,

**Table 5.** The fraction of 21-cm absorption detections (C) and the number density of 21-cm absorbers ( $n_{21}$ ) for the different 21-cm optical depth limits ( $\mathcal{T}_0$ ) using the homogeneous sample S1. N is the total number of systems in the sample with  $\int \tau_{3\sigma,10} dv \leq \mathcal{T}_0$ , and  $N_{21}$  is the number of 21-cm detections with  $\int \tau_{3\sigma,10} dv \leq \mathcal{T}_0$  and  $\int \tau dv \geq \mathcal{T}_0$ .

$z$ range	Sample	$\mathcal{T}_0$ ( $\text{km s}^{-1}$ )	Systems (N)	Detections ( $N_{21}$ )	C	$n_{21}$
1.1-1.5	Ours (i.e. This paper + G09)	0.10	8	4	$0.50^{+0.40}_{-0.24}$	$0.13^{+0.11}_{-0.06}$
		0.20	22	4	$0.18^{+0.14}_{-0.09}$	$0.05^{+0.04}_{-0.02}$
		0.30	27	3	$0.11^{+0.11}_{-0.06}$	$0.03^{+0.03}_{-0.02}$
		0.50	36	4	$0.11^{+0.05}_{-0.34}$	$0.03^{+0.01}_{-0.01}$
1.1-1.5	Ours + literature	0.10	10	5	$0.50^{+0.34}_{-0.22}$	$0.13^{+0.09}_{-0.06}$
		0.20	26	5	$0.19^{+0.13}_{-0.08}$	$0.05^{+0.04}_{-0.02}$
		0.30	32	4	$0.13^{+0.10}_{-0.08}$	$0.03^{+0.03}_{-0.02}$
		0.50	41	5	$0.12^{+0.08}_{-0.05}$	$0.03^{+0.02}_{-0.01}$
1.1-1.5	Ours + literature <i>with</i> VLBA (assuming $f_c = c_f$ )	0.10	4	2	$0.50^{+0.50}_{-0.32}$	$0.13^{+0.17}_{-0.09}$
		0.20	8	1	$0.13^{+0.29}_{-0.10}$	$0.03^{+0.07}_{-0.03}$
		0.30	10	1	$0.10^{+0.17}_{-0.08}$	$0.03^{+0.04}_{-0.02}$
		0.50	16	2	$0.13^{+0.17}_{-0.08}$	$0.03^{+0.04}_{-0.02}$
1.1-1.5	Ours + literature <i>with</i> VLBA (assuming $f_c = f_{VLBA}$ )	0.10	4	2	$0.50^{+0.50}_{-0.32}$	$0.13^{+0.17}_{-0.09}$
		0.20	8	1	$0.13^{+0.29}_{-0.10}$	$0.03^{+0.07}_{-0.03}$
		0.30	13	1	$0.08^{+0.18}_{-0.06}$	$0.02^{+0.05}_{-0.02}$
		0.50	17	3	$0.18^{+0.18}_{-0.10}$	$0.05^{+0.05}_{-0.03}$
0.5-1.0	Ours	0.10	4	1	$0.25^{+0.58}_{-0.21}$	$0.04^{+0.10}_{-0.04}$
		0.20	6	1	$0.17^{+0.38}_{-0.14}$	$0.03^{+0.07}_{-0.02}$
		0.30	8	1	$0.13^{+0.29}_{-0.10}$	$0.02^{+0.05}_{-0.02}$
		0.50	9	1	$0.11^{+0.26}_{-0.09}$	$0.02^{+0.04}_{-0.02}$
0.5-1.0	Ours + literature	0.10	20	3	$0.15^{+0.15}_{-0.08}$	$0.03^{+0.03}_{-0.02}$
		0.20	25	3	$0.12^{+0.12}_{-0.07}$	$0.02^{+0.02}_{-0.01}$
		0.30	28	3	$0.11^{+0.10}_{-0.06}$	$0.02^{+0.02}_{-0.01}$
		0.50	33	2	$0.06^{+0.08}_{-0.05}$	$0.01^{+0.01}_{-0.01}$
0.5-1.0	Ours + literature <i>with</i> VLBA (assuming $f_c = c_f$ )	0.10	5	2	$0.40^{+0.93}_{-0.32}$	$0.07^{+0.10}_{-0.06}$
		0.20	10	2	$0.20^{+0.29}_{-0.16}$	$0.04^{+0.05}_{-0.03}$
		0.30	12	2	$0.17^{+0.24}_{-0.14}$	$0.03^{+0.04}_{-0.02}$
		0.50	15	2	$0.13^{+0.20}_{-0.11}$	$0.02^{+0.03}_{-0.02}$
0.5-1.0	Ours + literature <i>with</i> VLBA (assuming $f_c = f_{VLBA}$ )	0.10	5	2	$0.40^{+0.58}_{-0.33}$	$0.07^{+0.10}_{-0.06}$
		0.20	11	2	$0.18^{+0.27}_{-0.15}$	$0.03^{+0.05}_{-0.03}$
		0.30	14	2	$0.14^{+0.21}_{-0.12}$	$0.03^{+0.04}_{-0.03}$
		0.50	15	2	$0.13^{+0.19}_{-0.11}$	$0.02^{+0.03}_{-0.02}$

J1252+4427 and J2031+1219. The subarcsecond scale images are available for 4 of these quasars (i.e. except J1252+4427) that are also amongst the brightest radio sources in our sample. As expected the estimated correction to account for the partial coverage is also large ( $c_f < 0.5$ ) for these. Despite this the 21-cm optical depth sensitivity achieved towards the ‘core’ component is exceptionally good (i.e.  $\int \tau_{3\sigma} dv \leq 0.2 \text{ km s}^{-1}$  even after correcting for the  $f_c$  assuming  $f_c = c_f$ ) for these 4 systems. The good optical depth sensitivity towards the milliarcsecond scale ‘core’ coupled with the large  $f_c$  correction ( $c_f < 0.5$ ) can be taken to imply that these quasars also have good optical depth sensitivity at the physical scales beyond ( $> 30 \text{ pc}$ )<sup>6</sup> the ‘core’ component. We notice that the 21-cm absorption in all these 5 cases exhibits large velocity widths i.e.  $\Delta V = 100\text{-}150 \text{ km s}^{-1}$ . Compared to this the widths of absorption lines towards the compact quasars plotted in the *top* panel of Fig. 7 are less than  $100 \text{ km s}^{-1}$ . This favours the idea that larger  $\Delta V$  observed towards the extended sources arise from the 21-cm absorbing gas that has transverse extent of  $> 30 \text{ pc}$ . We examine this further in the next Section.

<sup>6</sup> Based on the typical resolution at the absorber redshift achieved in the VLBA images used for ‘core’ identification.

#### 4.2. Correlations with VLBA morphological parameters

Now we explore the correlations between the VLBA morphological and 21-cm absorption parameters using the sample S2. In Fig. 8 we plot  $\int \tau dv / f_{VLBA}$  as the function of linear size. If we consider only those systems that are towards the quasars with the clear ‘core’ identification (plotted as circles in Fig. 8), we see that almost all the detections (except one) are towards the quasars with the linear size,  $LS < 100 \text{ pc}$ . However, the generalised rank correlation test suggests no correlation between the linear size and the  $\int \tau dv / c_f$ , or  $\int \tau dv / f_{VLBA}$ . The correlation between the linear size and  $\int \tau dv / f_{VLBA}$  is only significant at the level of  $0.4\sigma$  with a probability that it can arise due to a chance of 71%. The significance is even lower ( $0.1\sigma$ ) for the correlation between the linear size and  $\int \tau dv / c_f$ .

Now we return to the issue of relationship between the radio structure at subarcsecond scales and the width of 21-cm absorption lines. In Fig. 9 we plot the width of 21-cm absorption lines as the function of linear size measured from the VLBA maps for all the 21-cm detections from the sample S2. The only exception is the system towards J0804+3012 for which the linear size is measured from the subarcsecond scale images of Kunert et al. (2002). There are four systems in this figure showing  $\Delta V > 100 \text{ km s}^{-1}$ . These four are identified in Section 4.1 as

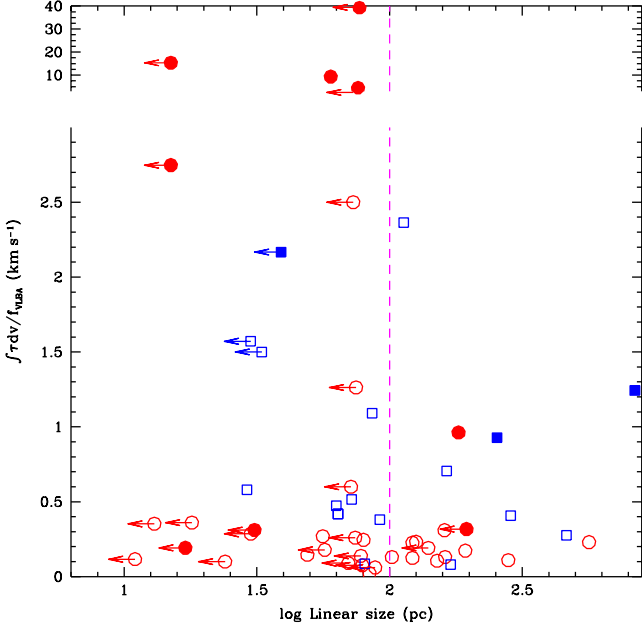


**Fig. 8.** Integrated 21-cm optical depth corrected for partial coverage assuming  $f_c = f_{VLBA}$  vs linear size (in pc) at the absorber redshift for the sample S2. Systems towards the quasars with no ‘core’ identifications are plotted as squares. 21-cm detections are shown as filled symbols where 21-cm non-detections are represented by open symbols. The point for the system towards B1629+120 with LS=7.2 kpc is not plotted to keep LS-axis short.

the ones towards the radio sources having extended morphology at arcsecond scales. It is also interesting to note that there are two systems with  $\Delta V \leq 40 \text{ km s}^{-1}$  towards the quasars that show extended morphology in the VLBA images (i.e J1058+4939 and B1629+120). The correlation analysis suggests only a weak correlation at the level of  $1.54\sigma$  with the probability that it can be by chance of 0.12.

The lack of strong correlation between  $\Delta V$  and projected linear size is not surprising. This is because, even if we only look at compact radio sources we expect a spread in the line of sight  $\Delta V$  as measured by the distribution of Mg II equivalent widths. Such line of sight velocity spread will dilute any possible correlation between  $\Delta V$  and LS that is expected to originate from the velocity gradients in the transverse direction as traced by the extended radio sources. In our sample, we do not find any correlation between  $W_r$  and  $\Delta V$ . The correlation analysis suggests a significance of  $0.27\sigma$  with a chance probability of 0.74. Note that Curran (2010) also finds only  $1.73\sigma$  correlation between  $W_r$  and  $\Delta V$  for a sample comprising both DLAs and  $W_r \geq 1 \text{ \AA}$  i.e. strong Mg II absorbers.

In summary, we find a large fraction of 21-cm detections to be towards the quasars having linear size  $\leq 100 \text{ pc}$  in the VLBA images. The largest velocity widths are seen towards the quasars that show extended structure at arcsecond scales. However, we do not find strong correlation between either  $\int \tau dv$  or  $\Delta V$  with the linear size measured from the milliarcsecond scale images. All this can be understood if the absorbing gas is patchy with a typical correlation length of  $\sim 30\text{-}100 \text{ pc}$ . It is quite likely that the narrow absorption components with the larger optical depths are associated with even smaller clouds (Srianand et al. in prep.).

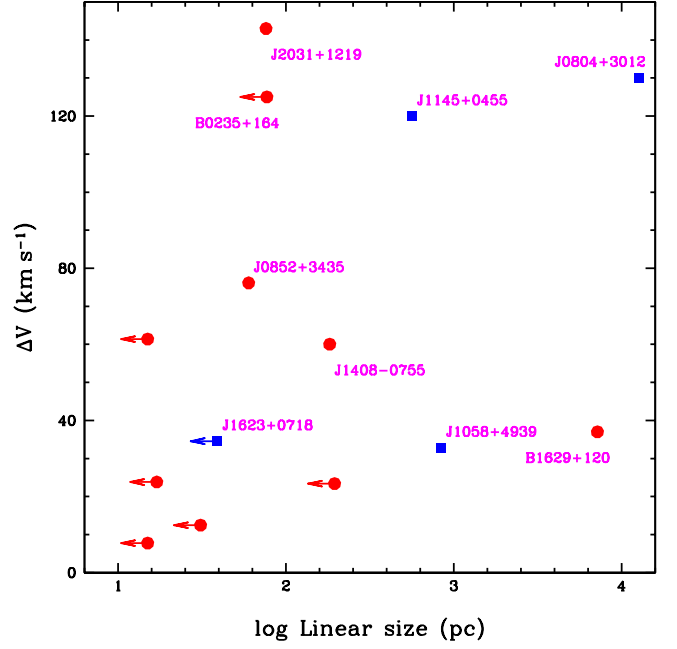


**Fig. 9.** Width ( $\Delta V$ ) of 21-cm absorption line in  $\text{km s}^{-1}$  is plotted against the linear size in pc measured from the VLBA maps. The systems towards the quasars with the ‘core’ identification are plotted as circles and the remaining are shown as squares.

#### 4.3. Milliarcsecond scale structure and 21-cm detection rate

In this Section, we determine the 21-cm detection rates for the strong Mg II absorbers after correcting the 21-cm optical depths for partial coverage. For this purpose, we will use the sample S1 that only consists of the systems primarily selected on the basis of  $W_r \geq 1 \text{ \AA}$  criterion as described in the Section 2.3. As noted above, if the 21-cm absorbing gas indeed extends beyond 30 pc then under the assumption of unit filling factor we can use  $c_f$  and  $f_{VLBA}$  to estimate  $f_c$  and obtain a realistic estimate of the optical depth sensitivity. As discussed in Section. 3, we have two possible values of  $f_c$  for 35 systems with ‘core’ identifications in the sample S1. Just to recollect, in the first case we assume  $f_c = c_f$ . The  $f_c$  in this case provides a conservative lower limit on the actual value of  $f_c$ . In the second case of  $f_c = f_{VLBA}$ , we assume that the absorbing gas extends over 300 pc to cover all the VLBA components. We determine the 21-cm absorption detection rates for these two scenarios using the corrected optical depth sensitivity limits. These detection rates for the different values of  $\mathcal{T}_0$  are summarised in Table 5.

It is clear from Table 5 that the detection rates in the low- $z$  bin are slightly higher in this case compared to the results obtained with no correction for the partial coverage. The slight gap noted between the low- and high- $z$  detection rates, when no correction for partial coverage is applied, is also reduced. The maximum increase in  $C$  after  $f_c$  correction is by a factor 2.7 for the low- $z$  bin. Thus covering factor is an important issue in measuring the redshift distribution of 21-cm absorption systems accurately. One may underestimate detection rate by up to factor  $\sim 2$  due to this effect alone.

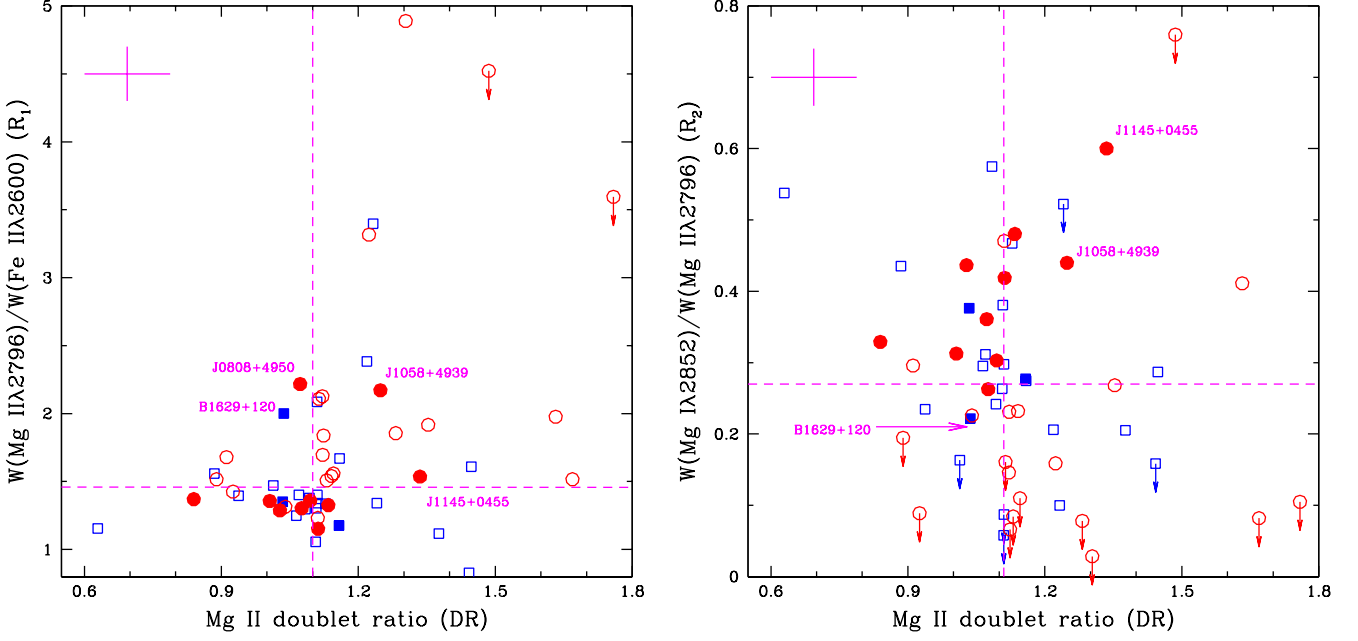


**Fig. 10.**  $R_1$  and  $R_2$  vs DR are plotted for the systems towards quasars with the VLBA images. Dashed lines in the panels are for median values of DR=1.1,  $R_1=1.47$  and  $R_2=0.27$ . Systems at  $0.5 < z < 1$  are plotted as squares and  $1.1 < z < 1.5$  as circles. Filled symbols are for 21-cm detections. Values for system towards J0808+4950 (G09), J1058+4939 (G09), J1145+0455 (Table C.1) and B1629+120 (Lane 2000) are labelled. Median error bars are shown at the top-left corner. System towards J2129–1538 is omitted due to large uncertainties on equivalent widths.

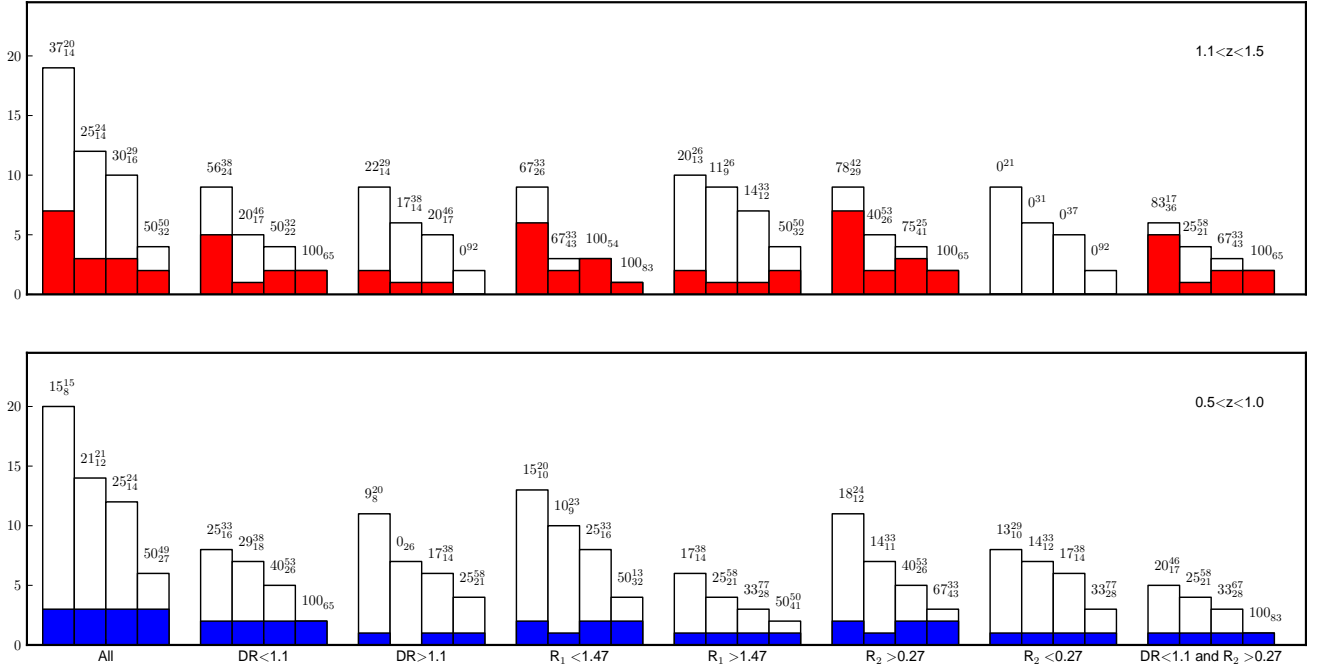


**Fig. 11.** Distribution of the number of Mg II systems for different subsamples from the sample S2 with the ‘core’ identification. Systems at  $1.1 < z < 1.5$  are plotted in the *top* panel and systems at  $0.5 < z < 1$  in the *bottom* panel. Shaded histogram corresponds to detections and optical depths have been corrected for partial coverage assuming  $f_c = c_f$ . For each subsample four bars correspond to no-cutoff,  $\mathcal{T}_o = 0.3$ ,  $0.2$  and  $0.1 \text{ km s}^{-1}$  respectively going from left to right. Detection rate,  $C$ , in each case is given at the top of bar.

## 5. 21-cm absorption and properties from their optical spectra

### 5.1. Metal absorption lines

It has been well established that the fraction of Mg II systems that are DLAs increases with the  $W_r$  (Rao et al. 2006). However, there exists a large scatter in the  $W_r$  and  $N(\text{H I})$  relationship, and  $W_r$  cannot be used as an indicator of the  $N(\text{H I})$  (Rao et al. 2011). On the other hand, the Mg II doublet ratio (DR),  $W(\text{Mg II } \lambda 2796)/W(\text{Fe II } \lambda 2600)$  (defined as  $R_1$ ) and  $W(\text{Mg I } \lambda 2852)/W(\text{Mg II } \lambda 2796)$  (defined as  $R_2$ ) can be used as a robust indicator of the presence of high  $N(\text{H I})$ . From the HST sample of Rao et al. (2006), we notice that  $27^{+9}_{-7}\%$  and  $38^{+15}_{-11}\%$  of the strong Mg II systems are DLAs at  $0.5 < z < 1.0$  and  $1.0 < z < 1.5$  respectively. The DLA fraction can be as high as 50% if further restrictions on the DR,  $R_1$  and  $R_2$  are imposed. G09 also noticed that a higher 21-cm detection rate can be obtained with the systems limited to a restricted range of these parameters.

In order to confirm if the 21-cm absorption detections occupy any preferred location in the parameter space defined by the metal absorption line ratios, we plot in Fig. 10 the ratios  $R_1$  and  $R_2$  as a function of DR. The Mg I, Mg II and Fe II equivalent widths for the systems taken from Kanekar et al. (2009) (see Table C.1) have been estimated using the SDSS and VLT archival spectra following the same procedure as done in G09 and Table 1. The equivalent widths for the systems that are from Lane (2000) are given in Table D.1. These have been taken from Lane (2000). When comparing the properties of the radio and optical absorption lines it is important to be able to address the issues that could arise due to the different gas volumes being probed by the radio and optical sight lines. For this reason, from the sample S2, we will consider here only the Mg II systems towards the quasars with the VLBA images.

It is clear from Fig. 10 that if we split the sample along the median values of DR,  $R_1$  and  $R_2$ , plotted as dashed lines, then  $\sim 75\%$  of the 21-cm detections have  $\text{DR} < 1.1$ ,  $R_1 < 1.47$  and  $R_2 > 0.27$ . The detection rate amongst the Mg II systems in the  $1.1 < z < 1.5$  sample, without any optical depth cut-off, is as high as 80% for these values of DR,  $R_1$  and  $R_2$ . This trend for  $1.1 < z < 1.5$  was previously noted by G09. Since 75% of the Mg II systems in the sample S2 at  $1.1 < z < 1.5$  considered here come from G09, this finding is not surprising. This result implies that the probability of detecting cold gas via 21-cm absorption is higher in systems with the high values of  $N(\text{H I})$ , and is consistent with the  $3\sigma$  level correlation between  $N(\text{H I})$  and  $T_s/f_c$  noted by Curran et al. (2010). A similar trend has also been noted for 21-cm detections in a sample of 28 bonafide DLAs at  $z > 2$  by Srianand et al. (2012).

In this context, it is interesting to recall that in the Section 2, we also presented 21-cm absorption measurements of the 4 Mg II systems i.e. towards the blazars J0457–2324, J1408–0752, J2031+1219 and J2129–1538, that were specifically selected on the basis of the metal absorption line properties that suggest that these systems may have H I column densities similar to the DLAs. The first three not only have  $W(\text{Mg II } \lambda 2796)/W(\text{Fe II } \lambda 2600) < 3/2$ , a criterion satisfied by the DLAs, they also have strong Mg I and Mn II absorption. The first two systems also show absorption lines of Zn II and Cr II. In the case of system towards J2129–1538, the absorption lines of Na I  $\lambda\lambda 3303.3, 3303.9$  are also detected. Detection of these species together with the Mg I, Mg II and Fe II suggest that the H I column densities should be significantly higher than the thresh-

old used to define DLAs. Therefore, high 21-cm detection rates towards these 4 blazars could be due to these systems having high  $N(\text{H I})$ .

Now we discuss the two deviations from the above mentioned trends. First, there are 3 21-cm detections in Fig. 10, labelled by the quasar name, that do not satisfy both the DR- $R_1$  and DR- $R_2$  values satisfied by the other 21-cm detections. The doublet ratio for system towards J1058+4939 is only  $1.5\sigma$  from the median dashed line of DR=1.1. It is interesting to note that the quasars J1058+4939, J1145+0455 and B1629+120 exhibit multiple radio components at sub-arcsecond scales. The dominant VLBA component for these three quasars is not ‘core’. Therefore it is possible that the radio and optical sight lines in these cases are probing different gas volumes resulting in the deviations seen in Fig. 10.

Second deviation is that at  $0.5 < z < 1$  only 20-30% of the systems with the  $\text{DR} < 1.1$ ,  $R_1 < 1.47$  and  $R_2 > 0.27$  are detected in the 21-cm absorption whereas at  $1.1 < z < 1.5$  this fraction can be as high as 80%. This cannot be attributed to the lower optical depth sensitivities achieved in the low- $z$  bin or the evolution of H I column density amongst the strong Mg II absorbers as the fraction of strong Mg II systems that are DLAs in the HST sample of Rao et al. (2006) are same at  $0.5 < z < 1$  and  $1.1 < z < 1.5$ . To examine this in detail we plot in Fig. 11, the distribution of systems in the sample S2 for the different subsets of Mg II systems defined on the basis of DR,  $R_1$  and  $R_2$ . For each subsample, the four histograms provide the number of systems and 21-cm detections for no optical depth cut-off, and  $\mathcal{T}_o = 0.3, 0.2$  and  $0.1 \text{ km s}^{-1}$  respectively. We have considered here only the subset of 39 systems with clear ‘core’ identifications, and the optical depths have been corrected for partial coverage assuming  $f_c = c_f$ . The trends observed in Fig. 11 are similar if we consider all the 56 systems with the VLBA maps and assume  $f_c = f_{\text{VLBA}}$  to correct for the partial coverage.

We stress here that the metal absorption line ratios measured from low resolution spectra such as SDSS considered here provide the properties averaged over several absorption components for a system. 21-cm absorption often arise from certain specific components (see e.g. Fig. 8 of Gupta et al. 2009). Also the error bars on individual DR,  $R_1$  and  $R_2$  measurements are large (see Fig. 10), and the observed deviations could simply be due to statistical fluctuations. Higher resolution optical spectra and most importantly  $N(\text{H I})$  measurements are required to address these issues.

### 5.2. Dust content

Most of the Mg II systems and DLAs in SDSS trace diffuse ISM and rarely show reddening due to dust in the spectra of individual quasars (Budzynski & Hewett 2011; Wild et al. 2006; York et al. 2006). However in the 21-cm absorption sample discussed in this paper, there are 4 Mg II systems selected from the SDSS that produce strong reddening signatures in the optical spectrum of the background quasar. Srianand et al. (2008) have discussed two of these systems ( $z_{\text{abs}} = 1.3265$  system towards J0850+5159 and  $z_{\text{abs}} = 1.3095$  towards J0852+3435) that show both the 2175 Å UV bump and 21-cm absorption. The other two systems that show strong signatures of the reddening due to dust but interestingly are not detected in the 21-cm absorption are discussed below.

1.  $z_{\text{abs}} = 1.3237$  system towards J0956+4046: This system is amongst one of the 12 high-confidence 2175Å absorber candidates of Jiang et al. (2011). In the top panel of Fig 12,

we show extinction curve fits to the SDSS spectrum of this object using the method described in Noterdaeme et al. (2009a). The observed spectrum is well fitted using LMC2 extinction curve and  $E(B-V) = 0.27$  and the bump strength (as defined by Jiang et al. 2011) of  $A_{\text{bump}} = 0.86$ . The main difference in our procedure is that we have fixed the wavelength and width of the 2175 Å feature as given by Fitzpatrick & Massa (2007). Using all the 491 QSOs with  $z_{\text{em}}$  within 0.004 to J0956+4046 we confirm the presence of bump at the high significance level (see left panels in Fig 12). If extinction per hydrogen atom in this system is similar to LMC then we expect  $N(\text{H I}) \sim 5 \times 10^{21} \text{ cm}^{-2}$ . The estimated  $E(B-V)$  value and rest equivalent widths of various species measured in this system are identical to the 21-cm absorber at  $z_{\text{abs}} = 1.3265$  towards J0850+5159 (Srianand et al. 2008) where the measured integrated 21-cm optical depth is  $15.3 \text{ km s}^{-1}$  (see Table 3 of G09). As shown in Fig. 1, J0956+4046 is resolved into two components in our GMRT image. The brightest component having a flux density of 53 mJy coincides with the optical position. A 21-cm absorber like the one we have seen towards J0850+5159 would have been easily detectable towards it. From Table B.1 we see that the  $3\sigma$  limit on  $\int \tau dv$  is  $0.35 \text{ km s}^{-1}$  for this component. This together with the above estimated  $N(\text{H I})$  value suggest that  $T_s/f_c > 7800 \text{ K}$ . In the case of high- $z$  CO absorbers  $E(B-V)/N(\text{H I})$  is found to be much higher (upto an order of magnitude) compared to what is seen in LMC (Noterdaeme et al. 2010a, Ledoux et al. in prep.). If we use the mean  $E(B-V)/N(\text{H I})$  found for the CO-DLAs whose SED is also well fitted with LMC2 extinction curve we get  $N(\text{H I}) \sim 4 \times 10^{20} \text{ cm}^{-2}$  and  $T_s/f_c > 600 \text{ K}$ . Therefore, the lack of 21-cm absorption could either be due to the covering factor of the gas being much less than 1 or the extinction per hydrogen atom in this absorber being much higher than that has been seen in LMC. As dusty regions are usually cold and the fact that our spectra is sensitive enough to detect the cold gas even when  $f_c$  is as low as 0.1 favours the second possibility. The multifrequency VLBA imaging of this source to constrain  $f_c$  and the  $N(\text{H I})$  measurement will provide important insights into this dusty Mg II system.

2.  $z_{\text{abs}} = 0.8620$  systems towards J1203+0634: Based on the presence of strong Ca II absorption and reddening, Wild et al. (2006) have suggested this system as a possible DLA candidate. We find that the SED can be well fitted with the SMC like extinction curve without any need for the presence of 2175 Å bump (See lower panel in Fig. 12). The equivalent width of Mg II and other species are like the other three systems mentioned above. The observed  $E(B-V)$  for SMC like dust-to-gas ratio corresponds to  $N(\text{H I}) > 10^{22} \text{ cm}^{-2}$ . Kulkarni et al. (2011) have reported a possible detection ( $3.6\sigma$  level) of  $10 \mu\text{m}$  Silicate absorption in this system. Interestingly Kanekar et al. (2009) have not detected 21-cm absorption despite having a very good  $\int \tau dv$  limit of  $0.07 \text{ km s}^{-1}$ . Lack of 21-cm detection in this system that has a high probability of having very large  $N(\text{H I})$  is interesting. Unlike J0956+4046, J1203+0634 is a strong radio source and all the flux density at arcsecond scales is recovered in the milliarcsecond scale VCS images at 2.3 GHz. The strongest VLBA component contains 66% of the total flux density. Rest of the flux is extended within 170 pc. Interestingly in the 8.4 GHz VLBA image the extended component is undetected and the unresolved component seen in the 2.3 GHz VLBA image resolves in to a core-jet structure over a LS of  $\leq 60 \text{ pc}$ .

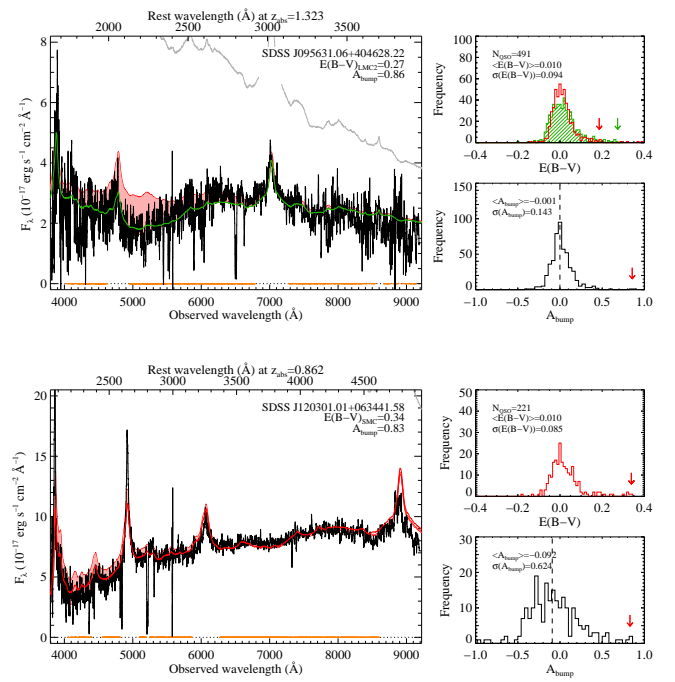


**Fig. 12.** Fitting the spectral energy distribution of J0956+4046 (top) and J1203+0634 (bottom). The SDSS spectrum (black) and the unreddened SDSS composite (gray) from Vanden Berk et al. (2001). The best extinction modelling is obtained for  $E(B-V)=0.27$  and a LMC2 extinction law for J0956+4046 (resp.  $E(B-V)=0.34$  and SMC law for J1203+0634) at the redshift of the absorber. The shaded area represents  $A_{\text{bump}}$ , the difference between the best model using Jiang et al. (2011) parametrisation with and without bump. The orange regions at  $y=0$  indicate the spectral range considered in the fitting process. The right panels show the distributions of  $E(B-V)$  (using SMC-law: red, LMC2: green hashed) and  $A_{\text{bump}}$  obtained for a control sample of SDSS QSOs (Schneider et al. 2010) within  $\Delta z = \pm 0.004$  from J0956+4046 (resp. J1203+0634). The arrows indicate the positions of the considered QSO.

Even if only 10% of the radio emission passes through the absorbing cloud the  $\int \tau dv$  limit achieved is sensitive enough to detect a  $T \sim 100 \text{ K}$  gas having  $N(\text{H I}) \sim 10^{20} \text{ cm}^{-2}$ . All this suggests that the lack of 21-cm absorption in this system may also be related to the extinction per H I atom being much higher than the Galaxy or SMC.

## 6. Discussion

### 6.1. Evolution of 21-cm detection rate and $n_{21}$

The nature of Mg II absorbers and their relationship with the galaxies has been a matter of debate. Recently [O II] emission, a measure of the star formation rate, has been detected in the individual as well as stacked SDSS spectra of the  $W_r > 0.7 \text{ \AA}$  Mg II absorbers (Noterdaeme et al. 2010b; Ménard et al. 2011). The average emission line luminosities are found to correlate with  $W_r$ . Ménard et al. (2011) show that Mg II absorbers not only trace a substantial fraction of the global [O II] luminosity density but also recover the overall star formation history of the Universe up to  $z \sim 2$ . They argue that this is suggestive of the scenario where most of the strong Mg II absorbers arise from the

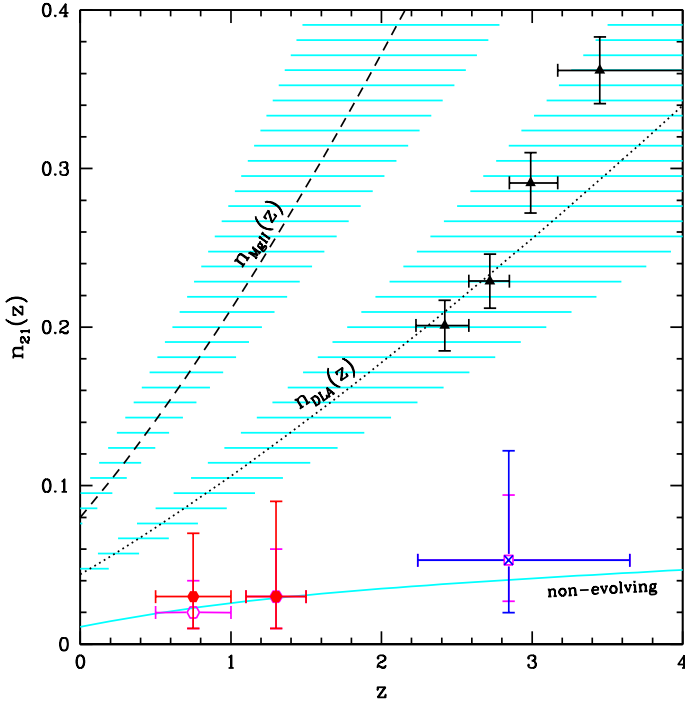


**Fig. 13.** Number of 21-cm absorbers per unit redshift range,  $n_{21}(z)$ , for  $\mathcal{T}_0 = 0.3 \text{ km s}^{-1}$ . Open circles are for no correction for partial coverage. Filled circles correspond to  $n_{21}$  after the optical depths have been corrected for partial coverage assuming  $f_c = c_f$ . The  $n_{21}$  based on DLAs at  $z > 2$  are plotted as squares and crosses with the latter corresponding to values after correcting for partial coverage. The curve for non-evolving population of 21-cm absorbers normalized at  $n_{21}(z = 1.3)$  is also plotted. Lines and dashed areas show the number of absorbers per unit redshift for DLAs (Rao et al. 2006, ; dotted line) and strong Mg II absorbers (Prochter et al. 2006, ; dashed line). Triangles are the number per unit redshift of DLAs measured from the sample of Noterdaeme et al. (2009b).

starburst driven galactic outflows (however see, López & Chen 2012, who suggest that the  $W_r$  vs.  $[\text{O II}]$  luminosity correlation can also be explained by the  $W_r$  vs. galaxy impact parameter anti-correlation and does not necessarily support the ‘outflow’ scenario).

Since the volume filling factor of different phases of ISM depends sensitively on the stellar feedback, in the ‘outflow’ scenario we expect CNM filling factor and the 21-cm detection rate of strong Mg II absorbers to evolve strongly with the starburst intensity (de Avillez & Breitschwerdt 2004). But in our analysis of the 21-cm absorption sample presented in the previous sections, we find that the 21-cm detection rate,  $C$ , is constant over the redshift range of  $0.5 < z < 1.5$  i.e. 30% of the age of Universe.

As described in G09, we can estimate the number density per unit redshift,  $n_{21}(\mathcal{T}_0, W_o, z)$ , of 21-cm systems with integrated optical depth  $\mathcal{T}_{21} \geq \mathcal{T}_0$  and Mg II equivalent width  $W_r \geq W_o$  from the number density per unit redshift of Mg II absorbers,  $n_{\text{MgII}}(W_o, z)$ , using the equation,

$$n_{21}(\mathcal{T}_{21} \geq \mathcal{T}_0, W_r \geq W_o, z) = C(z) \times n_{\text{MgII}}(W_r \geq W_o, z). \quad (2)$$

The  $n_{21}$  for different values of  $\mathcal{T}_0$  are given<sup>7</sup> in the last column of Table 5. In Fig. 13 we also plot the  $n_{21}$  for  $\mathcal{T}_0 = 0.3 \text{ km s}^{-1}$ . The constancy of  $C$  as a function of redshift implies that the  $n_{21}$  increases with redshift with a same slope as  $n_{\text{MgII}}$ . Due to the small number of positive 21-cm detections in Mg II systems the errors on  $n_{21}$  are large and on its own the estimates would also be consistent with the non-evolving population of 21-cm absorbers (Fig. 13). We conclude that the current data does not show any sign of the evolution of CNM filling factor of strong Mg II absorbers and  $n_{21}$  simply follows  $n_{\text{MgII}}$  over  $0.5 < z < 1.5$ . This is puzzling if the strong Mg II absorbers are indeed driven by the stellar feedback processes that tend to diminish the CNM filling factor.

## 6.2. Implications for 21-cm detection rates based on samples of DLAs at $z > 2$

Unlike strong Mg II absorbers that are often favoured to be associated with the galactic winds, DLAs are believed to probe the gas confined to the disks of galaxies. It is also interesting to note that, in contrast to the several Mg II host galaxy detections, the searches to detect DLA host galaxies have mostly resulted in null detections (e.g. Moller & Warren 1993; Fynbo et al. 2010; Rahmani et al. 2010; Fynbo et al. 2011; Bouché et al. 2012; Noterdaeme et al. 2012). Consequently DLAs are believed to correspond to low star-forming galaxies or trace the outer regions of extended H I disks far away from the star-forming regions (Rahmani et al. 2010). Given that a large fraction (~40%) of strong Mg II absorbers are likely to be DLAs, it is interesting to view the 21-cm detection rates derived for the Mg II systems in the context of 21-cm absorption searches based on bonafide DLAs.

Since at  $z \geq 2$ , Ly $\alpha$  can be observed from the ground based facilities the systematic searches of 21-cm absorption in DLAs have only been possible at  $z > 2$ . A summary of all the 28 DLAs searched for 21-cm absorption at  $2.0 \leq z_{\text{abs}} \leq 3.5$  is provided in Table 6 of (Srianand et al. 2012). Using the subsample of DLAs towards the quasars with the VLBA ‘core’ identifications from this Table, we estimate the 21-cm detection rate,  $C = 0.22^{+0.29}_{-0.14}$  for  $\mathcal{T}_0 = 0.3 \text{ km s}^{-1}$ . In Fig 5 we plot  $n_{21}$  corresponding to this. The method used is exactly similar to the one used for estimating  $n_{21}$  from Mg II systems in Section 6.1 except that the number per unit redshift range of DLAs ( $n_{\text{DLA}}$ ) is used in the place of  $n_{\text{MgII}}$  in Equation 2. The  $n_{\text{DLA}}$  required for this purpose has been measured from the DLA sample of Noterdaeme et al. (2009b).

Kanekar et al. (2009) used the detection rate of 21-cm absorption in Mg II systems and the fraction of Mg II systems that are DLAs to argue that the 21-cm detection rate in DLAs is strongly decreasing with redshift. In the  $W_r \geq 1 \text{ \AA}$  Mg II subsample with the VLBA ‘core’ identifications presented in this paper, the 21-cm detection rates at  $0.5 < z < 1$  and  $1.1 < z < 1.5$  for  $\mathcal{T}_0 = 0.3 \text{ km s}^{-1}$  and  $f_c = c_f$  correction are  $0.17^{+0.24}_{-0.14}$  and  $0.10^{+0.23}_{-0.08}$  respectively (Table 5). From the HST sample of Rao et al. (2006), the fraction of strong Mg II systems that are DLAs in these redshift bins are  $27^{+9}_{-7}\%$  and  $38^{+15}_{-11}\%$  respectively. If we assume that all the 21-cm detections are DLAs then the fraction of DLAs showing 21-cm absorption will be 0.63 and 0.26 respectively for the low- and high- $z$  bins. Since all the 21-cm detections need not be associated with the DLAs, these fractions should only be con-

<sup>7</sup>  $n_{21}$  for strong Mg II absorbers at  $0.5 < z < 1.5$  have been estimated by approximating  $n_{\text{MgII}}$  as,  $n_{\text{MgII}}(W_o, z) = n_0 \times (1+z)^\gamma$  with  $n_0 = 0.080^{+0.015}_{-0.005}$  and  $\gamma = 1.40 \pm 0.16$  for  $W_o = 1 \text{ \AA}$  (Prochter et al. 2006).



sidered as upper limits. The 21-cm absorption detection rate in the DLAs at  $z > 2$  is lower by at most a factor 3 compared to the upper limits we obtained using the  $W_r \geq 1 \text{ \AA}$  Mg II absorbers at  $0.5 < z < 1.0$ . However, at  $1.1 < z < 1.5$  the detection rate or the upper limit from the Mg II systems are consistent with the 21-cm detection rates from the DLAs at  $z > 2$ . This would imply that either the cross section of the 21-cm absorbing gas amongst DLAs has increased from  $z = 3.5$  to  $z = 0.5$  or that the significant fraction of 21-cm absorbers at  $0.5 < z < 1.0$  arise from sub-DLAs. The  $N(\text{H I})$  measurements of Mg II systems with good 21-cm optical depth limits will be useful to distinguish between these possibilities (see also Curran & Webb 2006; Curran 2012).

### 6.3. Caveats and future work

In previous sections, we presented results from 21-cm absorption line searches based on the sample of 85 strong Mg II absorbers at  $0.5 < z < 1.5$ . When no correction for the effect of partial coverage is incorporated we find that the 21-cm detection rate can be underestimated by as much as factor 2. Using milliarc-second scale VLBA maps for 53 quasars with 57 intervening absorption systems from this sample, we determined the realistic 21-cm optical depths and detection rates. This is the largest sample of 21-cm absorbers assembled at any redshift range, and we systematically take into account the effect of varying 21-cm optical depth sensitivity and partial coverage towards different quasar sight lines. Despite this the small number statistics still play a significant role and results are not without caveats.

First caveat is related to our assumption that  $f_c$  can be estimated from the VLBA continuum images at 20-cm and 13-cm, whereas the redshifted 21-cm observations are at the wavelengths longer by a factor 2-4 compared to these. The actual values of  $f_c$  are likely to be different at the observing frequency. It is not obvious if the effect of this assumption is to simply increase the scatter or produce systematic wavelength dependent offsets as one also needs to take into account the effect of finite resolution of the VLBA images when identifying ‘core’ and determining  $f_c$ . Given the sensitivity of current receivers and the difficulties involved with calibration, the low-frequency milliarc-second scale imaging and spectroscopy is possible only for a very few strong targets. The VLBI imaging at 20-cm or shorter wavelengths will be the optimal way to estimate  $f_c$  for the large samples as presented here. Therefore it will be valuable to determine the appropriateness of this method by measuring the filling factor and extent of the 21-cm absorbing gas via VLBI spectroscopy of  $z < 0.2$  21-cm absorbers that is possible with the currently available VLBI receivers.

Second caveat is related to the fact that the 21-cm absorption searches in the different redshift ranges are based on the samples of different atomic or ionic species which complicates the overall interpretation. For example, the samples at  $z > 2$  are based on the DLAs whereas at  $z < 2$  on the Mg II systems which selects both the DLAs and sub-DLAs. Measuring  $N(\text{H I})$  in the Mg II systems is important to address this issue. More importantly it is well known that the optical spectroscopic surveys such as SDSS are performed after the color selection of QSO candidates and are biased against the dusty sight lines that are relevant for the cold atomic and molecular absorption lines that can be searched at radio wavelengths (e.g., Carilli et al. 1998). Therefore, radio absorption line surveys based on the samples of optical absorption lines provide a very incomplete view of the evolution of the cold atomic and molecular gas in the galaxies. The blind searches of radio absorption lines are required to overcome this barrier

and eliminate the biases due to the pre-selection based on different atomic/ionic species. Such large spectroscopic surveys will be possible with the upcoming Square Kilometre Array (SKA) Pathfinder surveys such as APERTIF, ASKAP, EVLA and MeerKAT.

We finish with the following question: what is the relationship of the 21-cm absorbers with the galaxies? This link is required to establish the direct connection with the nearby galaxies that are detectable in H I 21-cm emission. Using 21-cm emission line maps of nearby galaxies, Zwaan et al. (2005) have concluded that sight-lines with  $\log N(\text{H I})(\text{cm}^{-2}) \geq 20.3$  occur with a median impact parameter,  $\rho < 7.8 \text{ kpc}$ . It is also clear from their Fig. 14 that when  $10 \text{ kpc} < \rho < 15 \text{ kpc}$  the probability of having high  $N(\text{H I})$  is roughly between 50% to 70%. Galaxies have been found within 20 kpc to the DLAs and 21-cm absorbers at  $z \leq 1.0$  (Rao et al. 2003, 2011). The redshift distribution of DLAs typically require  $\rho < 30 \text{ kpc}$  to be consistent with the observed luminosity function of galaxies (Steidel 1995). While these studies constrain typical impact parameter ranges where 21-cm absorption is likely to be detected, they do not tell much about the nature of 21-cm absorbers itself due to the lack of information on spin temperature. Therefore, observations of 21-cm absorption towards the bright radio sources at small impact parameters to the gas disks/halos of nearby galaxies are required to determine the 21-cm absorption cross section of the galaxies and understand the nature of 21-cm absorbers (Carilli & van Gorkom 1992; Gupta et al. 2010; Borthakur et al. 2011).

## 7. Summary

We have presented results from a systematic search of 21-cm absorption in a sample of 17 strong Mg II absorbers at  $0.5 < z_{\text{abs}} < 1.5$  using the GBT, GMRT and WSRT. This resulted in 4 new 21-cm detections. The VLBA 20-cm maps of 40 quasars with 42 intervening Mg II systems are also presented.

Combining 21-cm absorption measurements for 50 strong Mg II systems presented in this paper and Gupta et al. (2009) with the measurements from literature (Lane 2000; Kanekar et al. 2009), we assemble a sample of 85 strong Mg II absorbers at  $0.5 < z < 1$  and  $1.1 < z < 1.5$ . Using the milliarc-second scale VLBA maps for the 54 quasars with 57 intervening absorption systems from this sample, we estimated the actual 21-cm optical depths and detection rates after correcting for the partial coverage. In our detailed analysis of this 21-cm absorption sample, we have taken into account the effect of varying 21-cm optical depth sensitivity and the partial coverage towards different quasar sight lines. Our main results are summarized as follow:

1. The 21-cm detection rate is found to be higher towards the quasars with flat/inverted spectral index,  $\alpha < 0$ . More than 73% of the 21-cm detections are towards the sources with linear size,  $LS < 100 \text{ pc}$ . This may imply that the characteristic size of the absorbing gas is less than 100 pc. The low detection rate towards the quasars with the steeper  $\alpha$  are due to poor optical depth sensitivity towards the ‘core’ i.e. low covering factor,  $f_c$  of the absorbing gas.
2. We find that the largest velocity widths ( $\Delta V > 100 \text{ km s}^{-1}$ ) are mainly seen towards the quasars that show extended radio structure at arcsecond scales. However, we do not find any correlation between the integrated 21-cm optical depth,  $\int \tau dv$  or the width of 21-cm absorption line,  $\Delta V$  with the LS measured from the VLBA images. This suggests that the absorbing gas is patchy with a typical correlation length  $\sim 30\text{--}100 \text{ pc}$ .

3. We find that when no correction for the effect of partial coverage i.e. as estimated from the milliarcsecond maps is incorporated the 21-cm detection rate can be underestimated by as much as a factor of 2.
4. The 21-cm detection rate is constant over  $0.5 < z < 1.5$  i.e. 30% of the age of Universe. The constancy of  $C$  as a function of redshift implies that  $n_{21}$  increases with the redshift with a same slope as  $n_{\text{MgII}}$ . Due to the small number of positive 21-cm detections in Mg II systems the errors on  $n_{21}$  are large and on its own the estimates would also be consistent with a non-evolving population of 21-cm absorbers (Fig. 13). We conclude that the current data do not show any sign of the evolution of the CNM filling factor of strong Mg II absorbers and  $n_{21}$  simply follows  $n_{\text{MgII}}$  over  $0.5 < z < 1.5$ . This is intriguing given that the strong Mg II absorbers are believed to be driven by the stellar feedback processes that tend to diminish the CNM filling factor.
5. We find that the 21-cm absorption detection rate in the DLAs at  $z > 2$  is at most a factor of 3 less than the upper limits we obtained using the Mg II absorbers at  $0.5 < z < 1.0$ . This would imply that either the cross section of 21-cm absorbing gas amongst DLAs has increased from  $z = 3.5$  to  $z = 0.5$  or that a significant fraction of 21-cm absorbers at  $0.5 < z < 1.0$  arise from sub-DLAs.
6. We find that 75% of 21-cm detections have Mg II doublet ratio  $\leq 1.1$ ,  $W(\text{Mg I } \lambda 2852)/W(\text{Mg II } \lambda 2796) \geq 0.27$  and  $W(\text{Mg II } \lambda 2796)/W(\text{Fe II } \lambda 2600) \leq 1.47$ . This confirms our previous finding that the probability of detecting 21-cm absorption is higher in the systems with high  $N(\text{H I})$  (Gupta et al. 2009; Srianand et al. 2012), and is consistent with the  $3\sigma$  level correlation between  $N(\text{H I})$  and  $T_s/fc$  noted by Curran et al. (2010).
7. We present a detailed discussion on the non-detection of 21-cm absorption in the two dusty absorbers that produce substantial reddening to the background QSOs. This could be either related to the gas covering factor being low or to the extinction per hydrogen atom in these systems being much higher than what is seen in the SMC and LMC. We prefer the second possibility on the basis of larger extinction per hydrogen atom seen in some of the high- $z$  DLAs with CO detections.

We discuss caveats of our survey results. The analysis is mainly limited by the small number of 21-cm detections. 21-cm detections of the order of SDSS DLA sample (Noterdaeme et al. 2009b) will be possible with the upcoming SKA pathfinders. Blind searches of 21-cm absorption lines with these instruments will provide a complete view of the evolution of cold gas in galaxies and shed light on the nature of Mg II systems and DLAs, and their relationship with stellar feedback processes.

*Acknowledgements.* We thank C. Carilli, E. de Blok, D.J. Saikia and an anonymous referee for useful suggestions and comments. We thank GBT, GMRT, VLBA and WSRT staff for their support during the observations. GBT and VLBA are run by National Radio Astronomy Observatory. The VLBA data from 2010 were correlated using NRAO's implementation of the DiFX software correlator that was developed as part of the Australian Major National Research facilities Programme and operated under license. The National Radio Astronomy Observatory is a facility of the National Science Foundation operated under cooperative agreement by Associated Universities, Inc. GMRT is run by the National Centre for Radio Astrophysics of the Tata Institute of Fundamental Research. The WSRT is operated by the ASTRON (Netherlands Institute for Radio Astronomy) with support from the Netherlands Foundation for Scientific Research (NWO). We acknowledge the use of SDSS spectra from the archive (<http://www.sdss.org/>). Funding for the SDSS and SDSS-II has been provided by the Alfred P. Sloan Foundation, the Participating Institutions, the National Science Foundation, the U.S. Department of Energy, the National Aeronautics and Space Administration, the Japanese Monbukagakusho, the Max Planck

Society, and the Higher Education Funding Council for England. RS and PPJ gratefully acknowledge support from the Indo-French Centre for the Promotion of Advanced Research (Centre Franco-Indien pour la promotion de la recherche avancée) under Project N.4304-2.

## References

- Aldcroft, T. L., Bechtold, J., & Elvis, M. 1994, *ApJS*, 93, 1
- Barthel, P. D., Miley, G. K., Schilizzi, R. T., & Lonsdale, C. J. 1988, *A&AS*, 73, 515
- Barthel, P. D., Tytler, D. R., & Thomson, B. 1990, *A&AS*, 82, 339
- Barthel, P. D., Vestergaard, M., & Lonsdale, C. J. 2000, *A&A*, 354, 7
- Beasley, A. J., Gordon, D., Peck, A. B., et al. 2002, *ApJS*, 141, 13
- Bergeron, J. & Boissé, P. 1991, *A&A*, 243, 344
- Bergeron, J., Boissé, P., & Ménard, B. 2011, *A&A*, 525, A51+
- Bergeron, J., Petitjean, P., Aracil, B., et al. 2004, *The Messenger*, 118, 40
- Borthakur, S., Tripp, T. M., Yun, M. S., et al. 2011, *ApJ*, 727, 52
- Bouché, N., Murphy, M. T., Péroux, C., et al. 2012, *MNRAS*, 419, 2
- Bouché, N., Murphy, M. T., Péroux, C., et al. 2007, *ApJ*, 669, L5
- Bowen, D. V. & Chelouche, D. 2011, *ApJ*, 727, 47
- Briggs, F. H. & Wolfe, A. M. 1983, *ApJ*, 268, 76
- Budzynski, J. M. & Hewett, P. C. 2011, *MNRAS*, 416, 1871
- Carilli, C. L., Menten, K. M., Reid, M. J., Rupen, M. P., & Yun, M. S. 1998, *ApJ*, 494, 175
- Carilli, C. L. & van Gorkom, J. H. 1992, *ApJ*, 399, 373
- Chen, H.-W., Helsby, J. E., Gauthier, J.-R., et al. 2010a, *ApJ*, 714, 1521
- Chen, H.-W., Wild, V., Tinker, J. L., et al. 2010b, *ApJ*, 724, L176
- Churchill, C. W., Kacprzak, G. G., & Steidel, C. C. 2005, in *IAU Colloq.* 199: Probing Galaxies through Quasar Absorption Lines, ed. P. Williams, C.-G. Shu, & B. Menard, 24–41
- Condon, J. J., Hicks, P. D., & Jauncey, D. L. 1977, *AJ*, 82, 692
- Curran, S. J. 2010, *MNRAS*, 402, 2657
- Curran, S. J. 2012, *ApJ*, 748, L18
- Curran, S. J., Tzanavaris, P., Darling, J. K., et al. 2010, *MNRAS*, 402, 35
- Curran, S. J., Tzanavaris, P., Murphy, M. T., Webb, J. K., & Pihlström, Y. M. 2007, *MNRAS*, 381, L6
- Curran, S. J. & Webb, J. K. 2006, *MNRAS*, 371, 356
- Dallacasa, D., Bondi, M., Alef, W., & Mantovani, F. 1998, *A&AS*, 129, 219
- de Avillez, M. A. & Breitschwerdt, D. 2004, *A&A*, 425, 899
- Ellison, S. L., Churchill, C. W., Rix, S. A., & Pettini, M. 2004, *ApJ*, 615, 118
- Fitzpatrick, E. L. & Massa, D. 2007, *ApJ*, 663, 320
- Fynbo, J. P. U., Laursen, P., Ledoux, C., et al. 2010, *MNRAS*, 408, 2128
- Fynbo, J. P. U., Ledoux, C., Noterdaeme, P., et al. 2011, *MNRAS*, 413, 2481
- Gupta, N., Salter, C. J., Saikia, D. J., Ghosh, T., & Jeyakumar, S. 2006, *MNRAS*, 373, 972
- Gupta, N., Srianand, R., Bowen, D. V., York, D. G., & Wadadekar, Y. 2010, *MNRAS*, 408, 849
- Gupta, N., Srianand, R., Petitjean, P., et al. 2007, *ApJ*, 654, L111
- Gupta, N., Srianand, R., Petitjean, P., Noterdaeme, P., & Saikia, D. J. 2009, *MNRAS*, 398, 201
- Isobe, T., Feigelson, E. D., & Nelson, P. I. 1986, *ApJ*, 306, 490
- Jiang, P., Ge, J., Zhou, H., Wang, J., & Wang, T. 2011, *ApJ*, 732, 110
- Kacprzak, G. G. & Churchill, C. W. 2011, *ApJ*, 743, L34
- Kanekar, N. & Chengalur, J. N. 2003, *A&A*, 399, 857
- Kanekar, N., Prochaska, J. X., Ellison, S. L., & Chengalur, J. N. 2009, *MNRAS*, 396, 385
- Kulkarni, V. P., Torres-Garcia, L. M., Som, D., et al. 2011, *ApJ*, 726, 14
- Kunert, M., Marecki, A., Spencer, R. E., Kus, A. J., & Niezgodna, J. 2002, *A&A*, 391, 47
- Lane, W. 2000, PhD thesis, University of Groningen
- Ledoux, C., Petitjean, P., Fynbo, J. P. U., Møller, P., & Srianand, R. 2006, *A&A*, 457, 71
- López, G. & Chen, H.-W. 2012, *MNRAS*, 419, 3553
- Ménard, B., Wild, V., Nestor, D., et al. 2011, *MNRAS*, 417, 801
- Moller, P. & Warren, S. J. 1993, *A&A*, 270, 43
- Murphy, D. W., Browne, I. W. A., & Perley, R. A. 1993, *MNRAS*, 264, 298
- Murphy, M. T., Curran, S. J., Webb, J. K., Ménager, H., & Zych, B. J. 2007, *MNRAS*, 376, 673
- Neff, S. G. & Hutchings, J. B. 1990, *AJ*, 100, 1441
- Nestor, D. B., Johnson, B. D., Wild, V., et al. 2011, *MNRAS*, 412, 1559
- Noterdaeme, P., Laursen, P., Petitjean, P., et al. 2012, *A&A*, 540, A63
- Noterdaeme, P., Ledoux, C., Srianand, R., Petitjean, P., & Lopez, S. 2009a, *A&A*, 503, 765
- Noterdaeme, P., Petitjean, P., Ledoux, C., et al. 2010a, *A&A*, 523, A80
- Noterdaeme, P., Petitjean, P., Ledoux, C., & Srianand, R. 2009b, *A&A*, 505, 1087
- Noterdaeme, P., Srianand, R., & Mohan, V. 2010b, *MNRAS*, 403, 906

- Piner, B. G., Bhattarai, D., Edwards, P. G., & Jones, D. L. 2006, *ApJ*, 640, 196
- Prochter, G. E., Prochaska, J. X., & Burles, S. M. 2006, *ApJ*, 639, 766
- Quider, A. M., Nestor, D. B., Turnshek, D. A., et al. 2011, *AJ*, 141, 137
- Rahmani, H., Srianand, R., Noterdaeme, P., & Petitjean, P. 2010, *MNRAS*, 409, L59
- Rao, S. M., Belfort-Mihalyi, M., Turnshek, D. A., et al. 2011, *MNRAS*, 1155
- Rao, S. M., Nestor, D. B., Turnshek, D. A., et al. 2003, *ApJ*, 595, 94
- Rao, S. M., Turnshek, D. A., & Nestor, D. B. 2006, *ApJ*, 636, 610
- Rector, T. A. & Stocke, J. T. 2001, *AJ*, 122, 565
- Reid, R. I., Kronberg, P. P., & Perley, R. A. 1999, *ApJS*, 124, 285
- Saikia, D. J., Junor, W., Cornwell, T. J., Muxlow, T. W. B., & Shastri, P. 1990, *MNRAS*, 245, 408
- Schneider, D. P., Richards, G. T., Hall, P. B., et al. 2010, *AJ*, 139, 2360
- Srianand, R., Gupta, N., Petitjean, P., et al. 2012, *MNRAS*, 421, 651
- Srianand, R., Gupta, N., Petitjean, P., Noterdaeme, P., & Saikia, D. J. 2008, *MNRAS*, 391, L69
- Steidel, C. C. 1995, in *QSO Absorption Lines*, ed. G. Meylan, 139
- Swarup, G., Sinha, R. P., & Hilldrup, K. 1984, *MNRAS*, 208, 813
- Ulvestad, J., Johnston, K., Perley, R., & Fomalont, E. 1981, *AJ*, 86, 1010
- Vanden Berk, D. E., Richards, G. T., Bauer, A., et al. 2001, *AJ*, 122, 549
- White, R. L., Becker, R. H., Helfand, D. J., & Gregg, M. D. 1997, *ApJ*, 475, 479
- Wild, V., Hewett, P. C., & Pettini, M. 2006, *MNRAS*, 367, 211
- Wills, B. J., Wills, D., Evans, II, N. J., et al. 1992, *ApJ*, 400, 96
- Wolfe, A. M., Broderick, J. J., Johnston, K. J., & Condon, J. J. 1978, *ApJ*, 222, 752
- York, B. A., Kanekar, N., Ellison, S. L., & Pettini, M. 2007, *MNRAS*, 382, L53
- York, D. G., Khare, P., Vanden Berk, D., et al. 2006, *MNRAS*, 367, 945
- Zwaan, M. A., van der Hulst, J. M., Briggs, F. H., Verheijen, M. A. W., & Ryan-Weber, E. V. 2005, *MNRAS*, 364, 1467

**Table 4.** Results from the VLBA data

R.A.	Dec.	$z_{\text{abs}}$	rms	Id	S	r	$\theta$	a	b/a	$\phi$	$S_T$	$f_{\text{VLBA}}/c_f$	LS	$\alpha$
(J2000)	(J2000)		(mJy beam $^{-1}$ )		(mJy)	(mas)	(deg)	(mas)		(deg)	(mJy)		(pc)	
(1)	(2)	(3)	(4)	(5)	(6)	(7)	(8)	(9)	(10)	(11)	(12)	(13)	(14)	(15)
<b>VLBA parameters at 20-cm</b>														
01 08 26.8432	-00 37 24.060	1.3710	1.8	1	489	0	–	6.36	0.54	78	930	0.97/	554	0.38
				2	162	16.8	80	29.90	0.12	-78		0.53		
				3	58	33.1	88	21.35	0.29	-33				
				4	90	51.4	87	13.61	0.39	-84				
				5	106	65.3	79	21.71	0.64	-64				
01 54 54.3653	-00 07 23.231	1.1803	0.3	1	250	0	–	6.83	0.16	-38	264	0.95	<57	-0.65
				2	11	0	–	4.24	0.00	68		0.11/	113	0.68
02 14 52.2909	+14 05 27.455	1.4463	0.2	2	3	13.3	57	10.99	0.54	-23	6256	0.09*	84	-0.25
				1	4080	0	–	4.75	0.85	39		0.85/		
02 59 28.5155	-00 19 59.983	1.3370	0.3	2	1224	9.9	22	4.85	0.29	24	235	0.98	<30	-0.55
				1	231	0	–	3.51	0.36	-10		0.76/	63	0.35
07 42 37.3873	+39 44 35.629	1.1485	0.3	1	74	0	–	5.98	0.17	-27	114	0.65*	464	0.49
				2	13	7.6	155	6.65	0.83	0		0.65/		
07 48 09.4683	+30 06 30.533	1.4470	0.3	1	105	0	–	28.33	0.50	-85	231	0.65/	286	0.08
				2	20	30.1	0	14.31	0.00	-85		0.69*		
				3	24	28.8	135	71.92	0.23	-79		0.04*		
08 00 36.0269	+50 10 44.290	1.4146	0.3	1	81	0	–	4.22	0.04	33	118	0.81/	286	0.08
				2	14	33.6	24	16.1	0.19	19		0.69*		
08 02 48.4323	+29 17 34.211	1.3648	0.3	1	7	0	–	3.94	0.42	-72	195	0.04*	<33	0.88
08 08 39.6666	+49 50 36.529	1.4071	2.1	1	482	0	–	2.03	0.51	-53	930	0.52	<17	-0.25
08 15 34.1624	+33 05 29.010	0.8515	0.2	1	25	0	–	3.96	0.16	26	343	0.07	<30	0.59
08 17 10.5482	+23 52 23.970	1.3060	0.3	1	105	0	–	3.81	0.12	-65	215	0.84/	122	0.15
				2	71	5.92	-44	4.73	0.00	66		0.49		
				3	5	14.5	-89	6.67	0.00	53				
08 45 06.2503	+42 57 18.393	1.1147	0.3	1	164	0	–	2.20	0.55	46	218	0.75	<18	0.03
08 50 42.2438	+51 59 11.654	1.3265	0.2	1	65	0	–	1.80	0.10	-89	63	1.03	<15	0.02
08 52 44.7391	+34 35 40.521	1.3095	0.3	1	47	0	–	2.39	0.67	64	69	0.74/	60	-0.36
				2	4	7.1	-124	8.69	0.00	-57		0.68		
09 30 35.0851	+46 44 08.579	0.6216	0.4	1	171	0	–	11.4	0.11	23	336	0.63/	92	0.49
				2	40	13.5	-154	13.6	0.39	15		0.51*		
09 53 27.9565	+32 25 51.525	1.2372	0.3	1	78	0	–	4.13	0.28	-1	132	0.71/	161	0.14
				2	16	19.3	0	11.0	0.34	-1		0.59		
10 07 18.0731	+22 51 26.955	0.5602	0.2	1	150	0	–	8.16	0.52	-64	350	0.55/	49	0.54
				2	42	7.6	-112	17.8	0.45	-7		0.43		
10 58 13.0427	+49 39 36.046	1.2120	0.2	1	5	0	–	15.3	0.00	64	244	0.33/	840	0.70
				2	27	20.9	92	7.98	0.00	90		0.11*		
				3	23	35.8	97	5.26	0.00	-81				
				4	6	56.9	-99	22.7	0.00	64				
				5	20	66.7	-107	12.7	0.98	-62				
11 00 21.0333	+16 29 14.661	0.8540	0.4	1	201	0	–	3.20	0.41	9	265	0.76	<25	0.22

Table 4. continued.

R.A.	Dec.	$z_{\text{abs}}$	rms	Id	S	r	$\theta$	a	b/a	$\phi$	$S_T$	$f_{\text{VLBA}}/c_f$	LS	$\alpha$
(J2000)	(J2000)		(mJy beam <sup>-1</sup> )		(mJy)	(mas)	(deg)	(mas)		(deg)	(mJy)		(pc)	
(1)	(2)	(3)	(4)	(5)	(6)	(7)	(8)	(9)	(10)	(11)	(12)	(13)	(14)	(15)
11 26 57.6554	+45 16 06.286	1.3022	1.4	1	340	0	–	3.42	0.66	21	424	0.80	<24	-0.21
11 48 56.5677	+52 54 25.337	0.8306	0.2	1	53	0	–	1.97	0.65	-69	100	0.78/	56	0.38
				2	25	7.36	116	3.70	0.00	-75		0.53		
11 57 34.8393	+16 38 59.769	0.7624	0.6	1	845	0	–	1.65	0.00	-80	747	1.00	<12	-1.13
12 08 54.2565	+54 41 58.163	1.2110	1.1	1	228	0	–	2.24	0.34	-51	265	0.86	<11	0.04
12 13 32.1710	+13 07 20.892	0.7718	1.4	1	145?	0	–	4.96	0.44	12	1356	0.11	<37	0.45
12 32 56.6101	+57 22 14.208	1.3429	0.2	1	4	0	–	7.33	0.39	-45	115	0.17/	164	0.79
				2	15	19.3	-150	37.57	0.19	26		0.13*		
12 34 31.7244	+64 55 56.530	1.3739/	0.3	1	22	0	–	3.95	0.00	56	93	0.43/	64	0.49
		1.3829		2	18	7.5	0	10.14	0.74	23		0.24*		
13 00 36.4392	+08 28 02.887	0.8665	0.3	1	50	0	–	4.86	0.21	3	106	0.68/	173	0.34
				2	18	12.2	-178	6.32	0.26	24		0.47		
				3	4	22.4	-170	7.60	0.00	-20				
13 29 01.4156	+10 53 04.807	0.6715/	0.2	1	34	0	–	3.60	0.00	-79	121	0.33/	72,86	0.41
		1.1645		2	6	10.3	81	9.80	0.69	9		0.28*		
13 33 35.7804	+16 49 04.109	0.7448	0.4	1	217	0	–	2.49	0.00	25	421	0.76/	151	0.29
				2	101	20.6	21	12.8	0.14	22		0.52		
14 08 56.4815	-07 52 26.635	1.2753	0.4	1	233	0	–	2.24	0.53	43	612	0.79/	182	0.24
				2	150	7.14	-106	4.35	0.00	48		0.38		
				3	77	13.5	-118	11.6	0.00	-85				
				4	25	8.35	47	11.0	0.37	-18				
14 10 30.9982	+61 41 36.908	0.7596	0.2	1	104	0	–	1.78	0.92	40	118	0.88	<13	-0.41
14 30 09.7389	+10 43 26.865	1.2431	0.8	1	301	0	–	1.69	0.46	65	311	0.97	<14	-0.91
15 01 24.6285	+56 19 49.678	1.2788	0.3	1	36	0	–	1.69	0.70	86	182	0.31/	29	0.25
				2	21	3.4	-117	9.97	0.00	64		0.20*		
15 08 23.7169	+33 47 00.762	1.1650	0.3	1	123	0	–	12.48	0.15	-45	132	0.99/	126	0.61
				2	7	15.2	-37	10.44	0.00	0		0.93		
16 23 46.2300	+07 18 54.891	1.3350	0.3	1	30	0	–	4.64	0.89	24	72	<0.42*	39	0.82
16 36 38.1833	+21 12 55.558	0.8000	0.4	1	147	0	–	2.06	0.69	-83	392	0.52/	193	0.34
				2	38	8.75	108	3.64	0.50	-58		0.38		
				3	7	9.11	-121	8.63	0.00	-47				
				4	13	19.3	113	14.4	0.47	10				
20 31 54.9948	+12 19 41.363	1.1157	0.2	1	447	0	–	2.58	0.40	4	985	0.48/	76	-0.60
				2	23	9.26	-173	10.4	0.10	-28		0.45		
23 40 23.6695	-00 53 27.009	1.3603	0.3	1	106	0	–	1.71	0.46	16	117	0.91	<15	-1.20
23 58 10.8819	-10 20 08.624	1.1726	0.4	1	571	0	–	3.71	0.29	-12	770	0.74	<31	-0.70
<b>VLBA parameters at 13-cm based on images from VCS</b>														
04 57 03.1792	-23 24 52.020	0.8922	4.4	–	–	–	–	–	–	–	1760	0.63	<195	-0.16
11 45 21.3153	+04 55 26.690	1.3433	0.5	–	–	–	–	–	–	–	554	0.60/	254	+0.55
												0.32		
21 29 12.1759	-15 38 41.041	0.6628	1.0	–	–	–	–	–	–	–	990	0.89	<140	-1.04

**Notes.** Columns 1 and 2: right ascension and declination of the ‘component-1’ (see column 5) fitted to the quasar, respectively; Column 3: absorption redshift; Column 4: rms in the map in  $\text{mJy beam}^{-1}$ ; Column 5: component id; Column 6: flux of the component in mJy; Columns 7 and 8: radius and position angle of the component with respect to ‘component-1’, respectively; Column 9: major axis in mas of the Gaussian component fitted to characterise the milliarcsecond scale structure; Columns 10 and 11: axial ratio and position angle of the Gaussian component, respectively; Column 12: flux density in mJy from FIRST/NVSS ( $S_T$ ); Column 13: ratio of total flux density detected in VLBA map and  $S_T$  (called  $f_{\text{VLBA}}$ ). In case of quasars with the multiple Gaussian components the  $c_f$  i.e. the ratio of the flux density of the strongest component detected in the VLBA map and the  $S_T$  is also given.; Column 14: largest linear size (LS) i.e. separation between the farthest components of the quasar in pc at absorber redshift. For the quasars represented by a single Gaussian component we take major axis of the deconvolved component as the upper limit on quasar size; Column 15: spectral index,  $S \propto \nu^{-\alpha}$ , between the 20-cm and 50-cm/90-cm using flux densities from the arcsecond scale maps.

## Appendix A: Log of the 21-cm absorption observations.

**Table A.1.** Log for the GBT, GMRT and WSRT observations.

Quasar	Telescope	Date	Time (hrs)
J0457–2324	GBT	2010 Mar 12	0.8
J0800+5010	GMRT	2009 Jun 05	4.4
J0817+2352	GMRT	2009 Jun 23	2.4
J0930+4644	WSRT	2009 Aug 22	22
		2009 Aug 23	
		2009 Sep 06	
		2009 Sep 08	
J0956+4046	GMRT	2009 Aug 09	12
		2009 Aug 24	
J1007+2251	GBT	2009 Oct 15	4.4
	WSRT	2009 Oct 24	12
J1148+5254	GBT	2009 Oct 16	4.3
		2009 Nov 19	
		2010 Jan 08	
J1216+5843	GBT	2009 Nov 19	1.9
		2010 Feb 18	
	WSRT	2009 Aug 20	8.8
J1252+4427	GBT	2010 Jan 19	2.3
J1329+1053	GBT	2010 Mar 12	4.1
		2010 Mar 13	
		2010 Mar 15	
		2010 Mar 22	
	WSRT	2009 Sep 16	9.8
J1333+1649	GBT	2010 Jan 09	2.4
		2010 Mar 12	
J1408–0755	GMRT	2009 Jun 21	2.5
		2010 Jan 22 <sup>†</sup>	4.5
J1410+6141	GBT	2009 Sep 16	5.0
		2009 Sep 17	
		2009 Oct 16	
		2009 Oct 19	
J1501+5619	GMRT	2009 Aug 24	3.1
J1636+2112	GBT	2009 Sep 25	2.4
J2031+1219	GMRT	2009 Jun 05	2.8
J2129–1538	WSRT	2006 Jul 12	27
		2006 Jul 13	
		2006 Jul 17	

**Notes.** The last column gives the total on-source time. <sup>(†)</sup> Higher resolution spectrum of the absorber towards J1408–0755 to study the variability.

## Appendix B: Determining flux densities and 21-cm optical depths

For the quasars observed with the GBT<sup>8</sup> the rms confusion due to other radio sources in the beam can be the dominant effect that limits the accuracy with which flux density of the background quasar and therefore the 21-cm optical depth can be determined. We use interferometric images from our WSRT observations and literature to address this issue. First consider the two quasars with 21-cm absorption detections from the GBT data.

<sup>8</sup> GBT beam FWHM at 800 MHz, corresponding to the central frequency of PF1-800 receiver, is 15'. The rms confusion corresponding to this is 90 mJy.

**Table B.1.** Summary of our 21-cm absorption measurements. Listed from left to right are the quasar name, flux density in mJy at the redshifted 21-cm frequency, spectral resolution in km s<sup>-1</sup>, spectral rms in mJy beam<sup>-1</sup> channel<sup>-1</sup> at the resolution given in the previous column, 3 $\sigma$  optical depth limit for the spectra smoothed to 10 km s<sup>-1</sup>, and the integrated 21-cm optical depth or in case of non-detections the 3 $\sigma$  upper limit for a spectral resolution 10 km s<sup>-1</sup>.

Quasar	Flux	$\delta v$	rms	$\tau_{3\sigma,10}$	$\int \tau dv$
J0457–2324	2400	3.9	3.2	0.002	0.20 $\pm$ 0.02
J0800+5010	126	4.0	2.1	0.033	<0.33
J0817+2352	244	3.8	2.4	0.019	<0.19
J0930+4644	415	3.4	5.3	0.024	<0.24
J0956+4046(P1)	53	3.8	0.9	0.035	<0.35
J0956+4046(P2)	23	3.8	0.9	0.080	<0.80
J1007+2251	397	3.2	1.7	0.008	<0.08
J1148+5254	122	3.8	1.3	0.021	<0.21
J1216+5843	537	3.6	2.7	0.010	<0.10
J1252+4427	497	3.9	2.0	0.008	2.06 $\pm$ 0.13
J1329+1053	138	3.5	1.2	0.017	<0.17
J1333+1649	486	3.6	2.1	0.008	<0.08
J1408–0755	744	3.8	1.9	0.005	0.51 $\pm$ 0.05
	685	1.9	1.9	0.004	0.48 $\pm$ 0.04
J1410+6141	93	3.6	1.5	0.031	<0.31
J1501+5619	223	3.8	2.1	0.018	<0.18
J1636+2112	456	3.7	2.1	0.009	<0.09
J2031+1219	595	3.5	2.7	0.009	2.11 $\pm$ 0.15
J2129–1538	341	3.4	3.2	0.017	<0.17

For J1252+4427, in the FIRST catalogue, there are no strong ( $\geq 10$  mJy) sources within 15' and the total flux density due to other sources within the beam FWHM is only  $\sim 20$  mJy. This suggests that the confusion is not a serious issue for this quasar, and indeed the flux density estimated from our GBT observations matches within  $\sim 5\%$  with the estimate from the interpolation of flux densities from the FIRST (at 20-cm) and WENSS (at 92-cm) surveys. The other quasar with 21-cm detection i.e. J0457–2324 is a blazar and known to exhibit variability (see Section 2.2). We measure the flux density of 2.72 Jy from our GBT observations. The contribution due to other sources within the beam FWHM at 20-cm based on the NVSS is 384 mJy (no beam-correction). The 90% of contribution comes from a source that has a steep spectral index of 0.9. Assuming that this other source is not variable would imply that the flux density of J0457–2324 is 2.4 Jy (beam correction applied) at the redshifted 21-cm absorption frequency.

Now consider systems towards the quasars with no 21-cm detections from the GBT. The flux density estimates for J1007+2251, J1216+5843 and J1329+1053 at the redshifted 21-cm frequency are estimated from our WSRT observations which took place within 6 months of the GBT observations (Table A.1). For J1148+5254 and J1410+6141, the flux densities at the redshifted 21-cm frequency have been estimated by interpolating between the flux densities from the FIRST and WENSS surveys at 20-cm and 92-cm respectively. The flux densities for J1333+1649 and J1636+2112 have been determined using the FIRST and TXS surveys. Table B.1 lists the flux densities and optical depth values for all the Mg II systems observed.

## Appendix C: Strong Mg II systems selected from Kanekar et al. (2009)

**Table C.1.** Details of the strong Mg II systems ( $W_r \geq 1\text{\AA}$ ) and 21-cm absorption measurements taken from Kanekar et al. (2009). Listed from left to right are the quasar names, their emission redshifts, redshifts of the intervening Mg II systems, rest frame equivalent widths of the Mg II $\lambda$ 2796, Mg II $\lambda$ 2803, Mg II $\lambda$ 2852 and Fe II $\lambda$ 2600 absorption lines, integrated 21-cm optical depth or in case of non-detection the  $3\sigma$  upper limit to it for a spectral resolution of  $10\text{ km s}^{-1}$ , and quasar morphology at 1.4 GHz. The quasars are classified as compact (C) when deconvolved size in the FIRST is less than  $2''$  and resolved (R) when the deconvolved size  $> 2''$ . When the FIRST is not available, the classification is either based on the radio morphology from the references provided below or on the NVSS/SUMSS when nothing else is available. The last three columns give  $f_{VLBA}$ ,  $c_f$  and the largest linear size of the quasars estimated from the milliarcsecond scale resolution maps.

Quasar	$z_{em}$	$z_{abs}$	$W_r(\text{Mg II}\lambda 2796)$ ( $\text{\AA}$ )	$W_r(\text{Mg II}\lambda 2803)$ ( $\text{\AA}$ )	$W_r(\text{Mg II}\lambda 2852)$ ( $\text{\AA}$ )	$W_r(\text{Fe II}\lambda 2600)$ ( $\text{\AA}$ )	$\int \tau dv$ ( $\text{km s}^{-1}$ )	Mor.	$f_{VLBA}$	$c_f$	LS (pc)
<b>Systems at <math>0.5 &lt; z &lt; 1</math></b>											
B0039–407	2.478	0.8485	$2.47 \pm 0.01^V$	$2.34 \pm 0.01$	$0.56 \pm 0.01$	$1.90 \pm 0.01$	$< 0.49$	C <sup>1</sup>	–	–	–
B0109+176	2.157	0.8392	$1.75^B$	1.20	$< 0.20$	1.09	$< 0.039$	R <sup>2</sup>	–	–	–
B0240–060	1.805	0.5810	$1.90 \pm 0.02^V$	$1.38 \pm 0.02$	$0.39 \pm 0.03$	$1.70 \pm 0.02$	$< 0.075$	C <sup>1</sup>	1.00	1.00	$< 79$
	1.805	0.7550	$1.67 \pm 0.01^V$	$1.48 \pm 0.01$	$0.78 \pm 0.01$	$1.25 \pm 0.04^{E1}$	$< 0.061$	C <sup>1</sup>	1.00	1.00	$< 88$
B0244–128	2.201	0.8282	$1.66 \pm 0.01^V$	$1.56 \pm 0.01$	$0.49 \pm 0.01$	$1.33 \pm 0.01$	$< 0.13$	R <sup>3</sup>	1.00	0.92	162
B0409–045	1.684	0.8797	$1.58 \pm 0.22$	$1.16 \pm 0.21$	$< 0.23$	$1.21 \pm 0.20$	$< 0.14$	C <sup>1</sup>	–	–	–
B0445+097	2.108	0.8392	$3.17^B$	2.19	0.91	1.97	$< 0.054$	R <sup>2</sup>	0.22	0.17	80
B0812+332	2.426	0.8518	$2.67 \pm 0.28$	$2.19 \pm 0.31$	$0.55 \pm 0.15$	$1.12 \pm 0.27$	$< 0.11$	C	0.07	0.07*	$< 30$
B0957+003	0.905	0.6722	$1.96 \pm 0.16$	$1.57 \pm 0.17$	$0.32 \pm 0.16$	$1.15 \pm 0.24$	$< 0.06$	R	–	–	–
B1012+022	1.375	0.7632	$1.53 \pm 0.05$	$1.28 \pm 0.05$	$0.33 \pm 0.05$	$0.71 \pm 0.05$	$< 0.06$	R	–	–	–
B1200+068	2.182	0.862	$5.29 \pm 0.27$	$4.88 \pm 0.26$	$3.04 \pm 0.27$	$4.08 \pm 0.31$	$< 0.08$	C	1.00	0.66*	170
B1210+134	1.139	0.7717	$1.22 \pm 0.09$	$1.14 \pm 0.09$	$0.38 \pm 0.10$	$0.87 \pm 0.10$	$< 0.052$	C?	0.20	0.20	$< 74$
B1222+438	1.075	0.7033	$1.01 \pm 0.25$	$0.70 \pm 0.25$	$< 0.16$	$1.22 \pm 0.26$	$< 0.42$	R	0.70	0.70	$< 72$
B1324–047	1.882	0.7850	$2.62 \pm 0.02^V$	$2.36 \pm 0.01$	$0.78 \pm 0.02$	$1.87 \pm 0.02$	$< 0.48$	C?	0.38	0.38	$< 75$
B1343+386	1.852	0.8076	$1.61 \pm 0.12$	$1.45 \pm 0.12$	$< 0.14$	$1.20 \pm 0.12$	$< 0.06$	R	0.70	0.30*	81
B1402–012	2.518	0.8901	$1.14 \pm 0.09$	$1.03 \pm 0.09$	$0.30 \pm 0.10$	$1.08 \pm 0.09$	$< 0.09$	C	0.65	0.65	$< 78$
B1611+343	1.397	0.6672	$1.21 \pm 0.06$	$1.09 \pm 0.06$	$< 0.07$	$0.58 \pm 0.07$	$< 0.09$	C	1.00	1.00	$< 70$
B1701+593	1.798	0.7238	$1.67 \pm 0.22$	$1.17 \pm 0.22$	$0.80 \pm 0.20$	$1.24 \pm 0.24$	$< 0.10$	R	–	–	–
<b>Systems at <math>1.1 &lt; z &lt; 1.5</math></b>											
B1005–333	1.837	1.3734	$0.93^{E2}$	...	...	0.84	$< 0.11$	C <sup>1</sup>	1.00	0.78	280
B1136+408	2.366	1.3702	$1.37 \pm 0.21$	$0.69 \pm 0.23$	$< 0.23$	$0.60 \pm 0.23$	$< 0.13$	C	1.00	1.00?	102
B1142+052 <sup>†</sup>	1.345	1.3431	$2.15 \pm 0.11$	$1.61 \pm 0.12$	$1.29 \pm 0.14$	$1.40 \pm 0.17$	0.557	R	0.60	0.32	254
B1204+399	1.518	1.3254	$1.41 \pm 0.11$	$1.10 \pm 0.11$	$< 0.11$	$0.76 \pm 0.14$	$< 0.23$	C	1.00	0.72*	564
B2003–025	1.457	1.2116	$2.65 \pm 0.14^A$	$2.17 \pm 0.15$	$< 0.31$	$1.27 \pm 0.14$	$< 0.022$	R	–	–	–

**Notes.** <sup>(†)</sup> This system is common with G09. <sup>(V)</sup> Equivalent widths measured using VLT archival spectra. <sup>(B)</sup> Equivalent widths from Barthel et al. (1990). <sup>(1)</sup> Equivalent widths from York et al. (2007). <sup>(A)</sup> Equivalent widths from Aldcroft et al. (1994). <sup>(E1)</sup> Fe II $\lambda$ 2600 is not covered in the VLT UVES spectrum, the  $W_r(\text{Fe II}\lambda 2600)$  is taken from Ellison et al. (2004). <sup>(E2)</sup> Equivalent widths taken from Ellison et al. (2004). <sup>(1)</sup> Compact on the basis of NVSS/SUMSS. <sup>(2)</sup> Projected linear size  $> 2''$  at 5 GHz (Barthel et al. 1988). <sup>(3)</sup> Projected linear size  $> 2''$  at 5 GHz (Reid et al. 1999).



## Appendix D: Strong Mg II systems selected from Lane (2000)

The Table 6 of G09 lists strong Mg II systems with 21-cm measurements from Lane (2000). Only systems at  $z_{\text{abs}} > 0.5$  are considered here (see Section 2.3). The systems towards B0109+176 and B0957+003 are common with the sample of Kanekar et al. (2009) and are listed in the Table C.1 with the more sensitive optical depth limits. In addition to the absorber towards B1622+238, we have excluded the system towards the quasar B0827+243 as it is non-Mg II selected (see Lane 2000, for the details).

**Table D.1.** Sample of Mg II systems with  $W_r \geq 1\text{\AA}$  from Lane (2000). The column listings are same as in Table C.1.

Source	$z_{\text{em}}$	$z_{\text{abs}}$	$W_r(\text{Mg II}\lambda 2796)$ ( $\text{\AA}$ )	$W_r(\text{Mg II}\lambda 2803)$ ( $\text{\AA}$ )	$W_r(\text{Mg I}\lambda 2852)$ ( $\text{\AA}$ )	$W_r(\text{Fe II}\lambda 2600)$ ( $\text{\AA}$ )	$\int \tau dv$ ( $\text{km s}^{-1}$ )	Mor.	$f_{\text{VLBA}}$	$c_f$	LS (pc)
B0109+200	0.746	0.5346	2.26	1.71	–	–	<0.27	C <sup>1</sup>	–	–	–
B0229+341	1.240	0.7754	1.92	2.02	<1.13	–	<0.43	R <sup>3</sup>	–	–	–
B0235+164	0.940	0.5238	2.42	2.34	0.91	1.79	13.0 <sup>†</sup>	R <sup>4</sup>	0.3-1	0.3-1	<77
B0420–014	0.915	0.6330	1.02	0.86	<0.36	–	<1.59	C <sup>5</sup>	–	–	–
B0454+039	1.343	0.8597	1.53	1.40	0.37	1.11	<0.11	C	0.88	0.55	122
B0805+046	2.876	0.9598	1.01	0.83	<0.60	0.24	<0.71	R <sup>2</sup>	–	–	–
B1218+339	1.519	0.7423	1.34	1.08	<0.70	1.00	<0.20	R	0.07	0.07	<73
B1327–206	1.169	0.8530	2.11	1.48	<0.40	0.76	<2.04	C <sup>1</sup>	–	–	–
B1354+258	2.004	0.8585	1.00	0.86	<0.10	<0.20	<1.05	R	–	–	–
B1556–245	2.815	0.7713	2.07	1.91	1.07	<0.20	<0.68	C <sup>6</sup>	–	–	–
B1629+120	1.795	0.5313	1.40	1.35	0.31	0.70	0.49 <sup>‡</sup>	C	0.30	0.10	7165 <sup>7</sup>
	”	0.9004	1.06	0.67	0.44	0.63	<0.82	C	–	–	–
B2212–299	2.703	0.6329	1.26	1.00	0.36	–	<2.07	C <sup>1</sup>	–	–	–

**Notes.** <sup>(†)</sup> 21-cm absorption data are from Wolfe et al. (1978). <sup>(‡)</sup> 21-cm absorption data are from Kanekar & Chengalur (2003). <sup>(1)</sup> Compact on the basis of NVSS. <sup>(2)</sup> Projected linear size  $> 2''$  at 5 GHz (Barthel et al. 1988). <sup>(3)</sup> Based on Swarup et al. (1984). <sup>(4)</sup> Based on the 1.64 GHz image from Murphy et al. (1993). <sup>(5)</sup> Unresolved in the  $3''$  scale resolution VLA image at 1.4 GHz (Ulvestad et al. 1981). <sup>(6)</sup> Compact in the 5 GHz images from Reid et al. (1999) and Barthel et al. (2000). <sup>(7)</sup> Based on 2.3 GHz image from Dallacasa et al. (1998); see Saikia et al. (1990) for the subarcsecond scale image at 408 MHz.

**Appendix E: 20 cm VLBA maps of quasars from our sample**

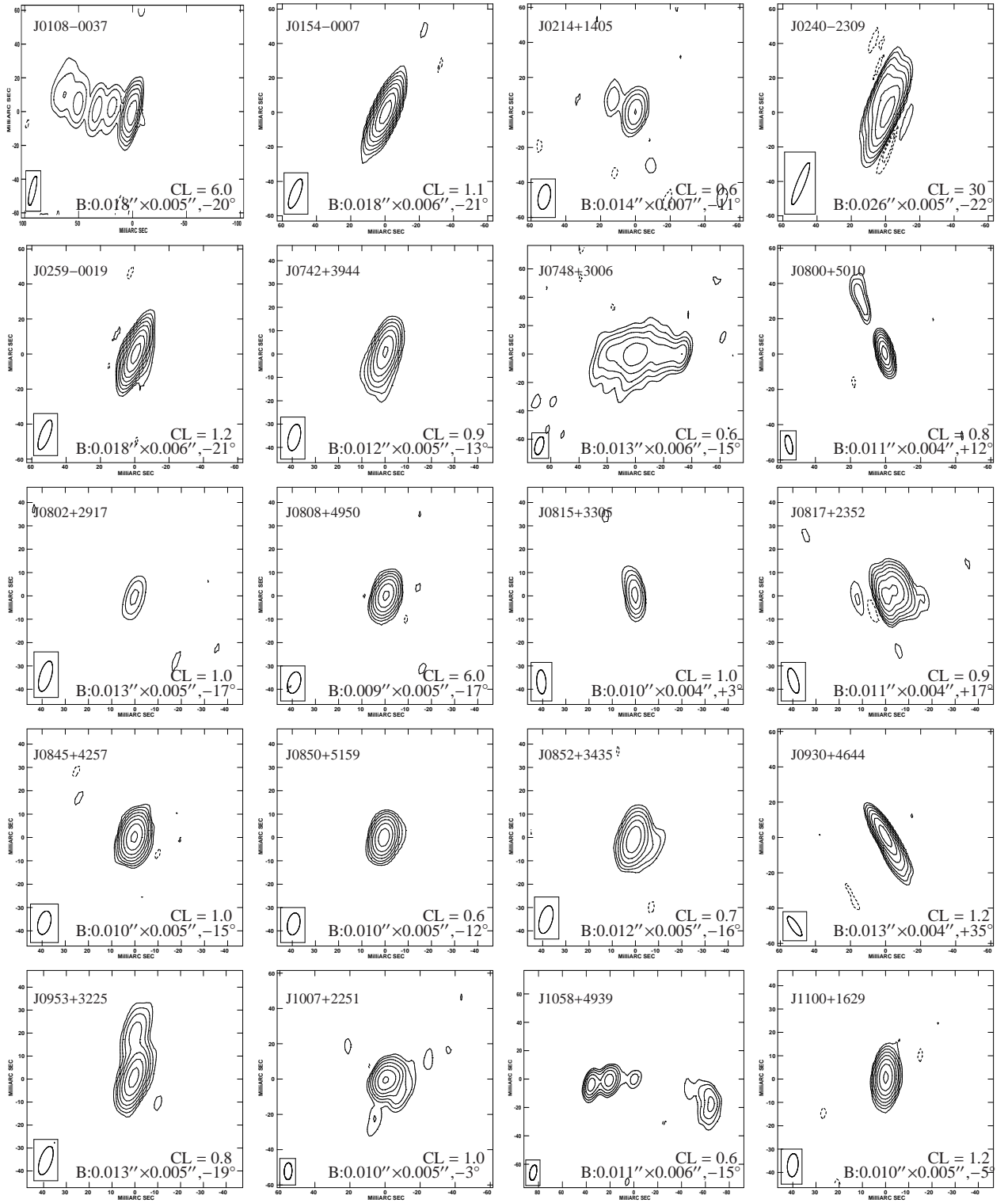


**Fig. E.1.** Contour plots of the VLBA images at 20 cm. The rms in the images are listed in Table 4 and the maps are centred at the Gaussian ‘component-1’ fitted to characterise the milliarcsecond scale structure. The restoring beam, shown as the ellipse, and the first contour level (CL) in mJy beam<sup>-1</sup> are provided at the bottom of each image. The contour levels are plotted as CL × (-1, 1, 2, 4, 8, ...) mJy beam<sup>-1</sup>.

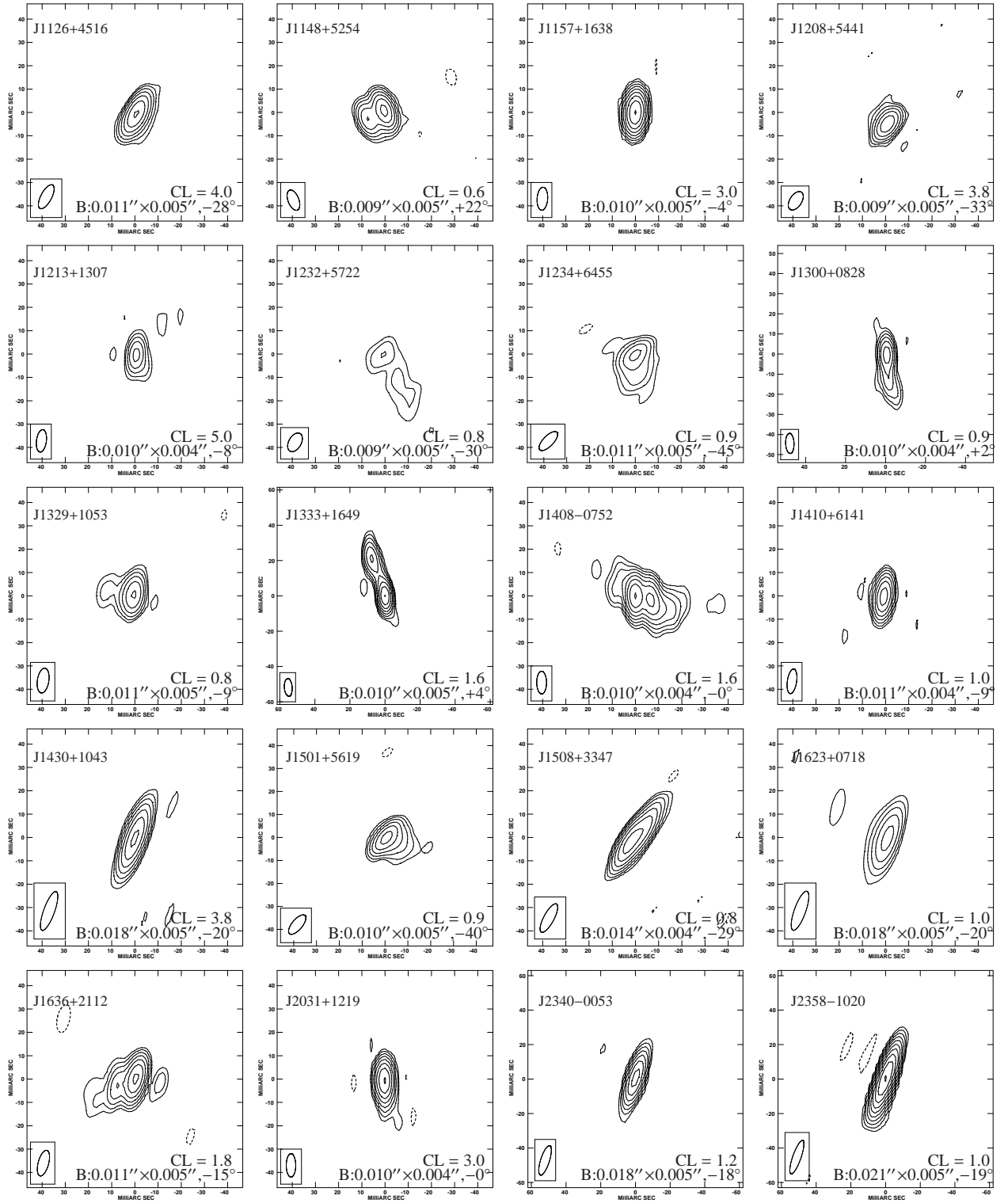


Fig. E.1. *Continued.*